Final Technical Report

Project Title: Imaging a Dry Storage Cask with Cosmic Ray Muons

Covering Period: October 2014 through December 2017

Date of Report: Mar. 31, 2018

Recipient: Oregon State University

B308 Kerr Administration Corvallis, OR 97331

Identification Number: DE-NE0008292

Principal Investigator:

Haori Yang, 541-737-7057, haori.yang@oregonstate.edu

Co-PI: Jason Hayward, University of Tennessee, Knoxville (UTK);

David Chichester, Idaho National Laboratory (INL)

Graduate Students:

Can Liao, <u>liaoc@oregonstate.edu</u> Zhengzhi Liu, <u>zliu36@vols.utk.edu</u>

Project Objective:

The goal of this project is to build a scaled prototype system for monitoring used nuclear fuel (UNF) dry storage casks (DSCs) through cosmic ray muon imaging. Such a system will have the capability of verifying the content inside a DSC without opening it. Because of the growth of the nuclear power industry in the U.S. and the policy decision to ban reprocessing of commercial UNF, the used fuel inventory at commercial reactor sites has been increasing. Currently, UNF needs to be moved to independent spent fuel storage installations (ISFSIs), as its inventory approaches the limit on capacity of on-site wet storage. Thereafter, the fuel will be placed in shipping containers to be transferred to a final disposal site. The ISFSIs were initially licensed as temporary facilities for ~20-yr periods. Given the cancellation of the Yucca mountain project and no clear path forward, extended dry-cask storage (~100 yr.) at ISFSIs is very likely. From the point of view of nuclear material protection, accountability and control technologies (MPACT) campaign, it is important to ensure that special nuclear material (SNM) in UNF is not stolen or diverted from civilian facilities for other use during the extended storage.

This project will be divided into the following six major tasks:

- A literature survey on the current state-of-knowledge related to muon imaging
- Design of a prototype that could be implemented on a real cask at an ISFSI
- Monte Carlo simulation to evaluate the performance of the prototype design
- Systematic study and optimization of image reconstruction techniques
- Experimental study with a scaled version in the laboratory
- Final field trials at the national laboratory partner's facility

Contents

\boldsymbol{C}	Contents	3
1.	Introduction	5
1.1.	Background	5
<i>1.2</i> .	Significance of study	5
2.	Theory and methodology	6
2.1.	Muon basics	6
2.2.	Image reconstruction algorithms	6
<i>3</i> .	Literature review on muon imaging	7
3.1.	Muon imaging techniques	7
<i>3.2.</i>	Muon imaging simulations	12
3.3.	Muon detectors	
<i>3.4.</i>	Plastic scintillator and light readout options	14
3.5.	MAPMT readout circuits	
4.	Preliminary simulation studies	
<i>4.1</i> .	Simulation study on energy deposited by muons in EJ-200 scintillators	16
4.2.	Muon imaging based on transmission – 2D	17
<i>4.3</i> .	Muon imaging based on scattering – 3D	
4.3.1	1. Modeling of simple geometries with POCA	
4.3.2	2. Modeling of a simplified DSC	19
<i>4.4</i> .	Modeling detailed DSC	19
<i>5</i> .	System design and characterization	22
<i>5.1</i> .	System design v1	23
5.1.1	1. Position calibration of position-sensitive detector v1	26
5.1.2	2. Integration test of v1	30
5.1. 3	3. Debugging system design v1	32
<i>5.2.</i>	System design v2	
5.2.1	1. Preliminary tests of system v2	37
5.2.1	1.1. Dark count measurement	37
5.2.1	1.2. Dynode signals measurement	39
5.2.1	1.3. Coincidence rate measurement	39
5.2.1	1.4. 2D position calibration of position-sensitive detector v2	40
5.2.2	2. Integration test of system v2	
5.2. 3	3. Imaging simple objects with system v2	44
5.2.4	4. Study of the impact of additional radiation	44

6.	Muon computed tomography algorithm studies	47
<i>6.1.</i>	Proposed framework for muon CT	48
6.1.1	Projection information	48
<i>6.2.</i>	Muon tracing methods	50
6.2.1	Method 1: Use of a straight path along the incident muon trajectory	50
6.2.2	. Method 2: Use of a straight path along the muon incident direction that crosses the PoCA point	51
6.2.3	Method 3: Use of PoCA trajectory	51
6.2.4	Method 4: Most probable trajectory	52
<i>6.3</i> .	Image reconstruction	53
<i>6.4</i> .	Validation & code benchmarking	54
6.4.1	Validation against experimental results	54
6.4.2	Code benchmarking using analytical data	55
<i>6.5.</i>	Results and discussion	56
6.5.1	Test model configuration	56
6.5.2	Results	57
6.6.	Detector size	62
<i>7</i> .	Summary and Conclusion	63
8.	Presentations and publications	63
9.	Training of graduate and undergraduate students	64
Refe	rence	65

1. Introduction

1.1. Background

Because of the growth of the nuclear power industry in the U.S. and the policy decision to ban reprocessing of commercial spent nuclear fuel, the used fuel inventory at commercial reactor sites has been increasing. Spent nuclear fuels at commercial power plants are firstly stored in onsite spent fuel pool for initial cooling down. As the inventory of spent nuclear fuel approaches the limit on capacity of on-site wet storage, it needs to be moved to independent spent fuel storage installations (ISFSIs). Thereafter, the fuel will be placed in shipping containers to be transferred to final disposal sites. The ISFSIs were initially licensed as temporary facilities for ~20-yr periods. Given the cancellation of the Yucca Mountain project and no clear path forward, extended dry-cask storage (~100 yr.) at ISFSIs is very likely. From the point of view of nuclear material protection, accountability and control technologies (MPACT) campaign, it is important to ensure that special nuclear material (SNM) in spent nuclear fuel is not stolen or diverted from civilian facilities for other use during the extended storage.

1.2. Significance of study

Dry cask storage is a method of storing high-level radioactive waste, such as spent nuclear fuel that has already been cooled in the spent fuel pool for at least one year and often as much as ten years. A very large amount of plutonium under nuclear safeguards is contained in spent nuclear fuel assemblies stored in DSCs (dry storage casks). These assemblies are practically inaccessible for monitoring purposes. Reopening a cask would require special facilities and would be tremendously expensive. Currently, there is no practical method to verify the content in a cask. Thus, containment and surveillance instrumentation has to be implemented to avoid loss of knowledge of the content. A method to verify the content in a cask is extremely important to the national interests. Thus, we believe this work is significant in homeland security and nonproliferation issues.

Conventional radiography techniques have achieved remarkable applications in various areas, but they have some limitations and disadvantages. X-rays and γ-rays can be easily stopped by dense and thick objects, while neutron are easily absorbed or scattered in low-Z material. Charged particles, such as electrons and protons, even with very high energy, which can only be achieved with high cost, can't penetrate thick high-Z materials like Uranium. Moreover, all the above types of radiation may bring health risk to the operators with inappropriate operation. Cosmic-ray muon radiography has been studied in the past years and was demonstrated to be a good non-destructive assessment of high-Z materials, such as spent nuclear fuel assemblies [1-3]. Thus, its application in Special Nuclear Materials (SNM) detection is very popular these years. Compared to conventional radiography techniques, muon radiography is safer due to its negligible health risk.

For the inspection of the interior contents of DSCs, one would prefer to use a passive technique which is simple to deploy and operate. The challenge is then complicated by limited accessibility, thick shielding and yet an intense mixed field radiation background. Muons at sea level have an average energy between 3 and 4 GeV, which makes them highly penetrating. The

average muon flux at sea level is about 1 cm⁻²·min⁻¹. Their high penetrating power, detectability and natural abundance make muons attractive particles for imaging large-volume objects. Muon radiography (transmission imaging) was then extended by tracking individual muons as they enter and exit the volume of interest. This has enabled reconstruction of the 3D distribution of matter inside the volume, i.e., tomography. Recently muon imaging has been used to detect nuclear threats for both homeland security and safeguard applications. In this work, we propose to utilize this technology for monitoring of DSCs.

2. Theory and methodology

2.1. Muon basics

Muons are generated when cosmic rays bombard the upper part of the earth's atmosphere. Muon flux reaching the surface of the Earth is about 10,000 muons per minute per square meter, which makes muons the most numerous cosmic-ray particles at sea level. The mean energy of muons at sea level is about 4 GeV. The angular distribution of muons in the GeV energy range is proportional to $\cos^2\theta$, where θ is the traveling direction of muons relative to the vertical direction, i.e. the polar angle in the spherical coordinate system. At lower energies, the angular distribution becomes increasingly steep, while at higher energies, it tends to flatten. Thus, cosmic-ray muon tomography is normally proposed to use near azimuthal angles (60° - 80° from the zenith) to obtain sufficient muon flux [4].

Similar to all the charged particles, Muons interact with matter via the weak and electromagnetic forces, mainly the Coulomb scattering. They travel relatively long distances while losing their kinetic energy and finally decay into an electron, a neutrino and an antineutrino. In materials, Muons undergo a random walk in direction, which conforms to a Gaussian angular distribution with a standard deviation:

$$\theta_0 = 13.6 \frac{\text{MeV}}{\text{\beta cp}} \sqrt{\frac{L}{L_0}} (1 + 0.038 \ln{\left(\frac{L}{L_0}\right)})$$
 (1)

where p is the muon's momentum in MeV/c and βc is its velocity. L₀, a muon's radiation length through a material, decreases rapidly as the atomic number (Z) of a material increases, which leads to an increased θ_0 . It can be observed that the spread of scattering angles is larger for materials with high atomic numbers and small radiation lengths. Therefore, the spread of the deflection angle of scattered muons provides a way to distinguish high-Z materials in the volume of interest. For example, in a 10 cm thick layer, a 3 GeV muon will scatter with an angular spread of 2.3 mrad in water but 20 mrad in tungsten [2]. The material can be mapped with its atomic number by measuring the width of the distribution of scattering angles obtained from each individual muon event.

2.2. Image reconstruction algorithms

The most commonly used and easiest algorithm used for 3-D image reconstruction is the Point of Closest Approach. It ignores multiple coulomb scattering and assumes a muon scattered at a single point [2]. Based on the direction and position information on the incident side and the

outgoing side, the scattering point is estimated as the midpoint of the line segment between the closest points on the two straight lines. The scattering angle is evaluated by taking the scalar product of the incident and outgoing muon momentum vectors. This is illustrated in Figure 1 [5].

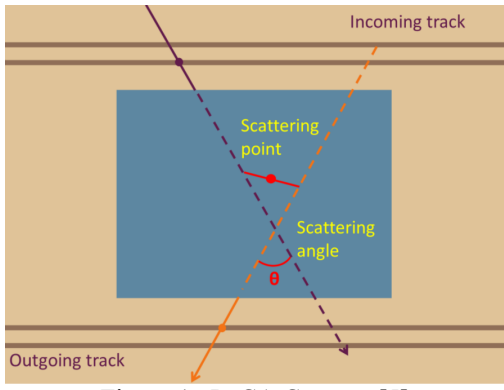


Figure 1. PoCA Concept [5]

In 2006-2007, Larry J. Schultz et al. introduced a maximum likelihood/expectation maximization tomographic reconstruction algorithm, which was then widely used in 3-D image reconstruction for muon tomography. A discrete tomographic reconstruction of the volume of interest is performed based on the data provided by many muons. They use an instance of the iterative expectation maximization (EM) algorithm to find maximum likelihood estimates of density profiles of objects. The use of EM algorithm, which is flexible and computationally efficient in addition to the Newton method to calculate maximum likelihood, is due to the stochastic scattering angle and the tortuous trajectories of muons [6]. The density profile is defined as the scattering density:

$$\lambda = \left(\frac{15}{p_0}\right)^2 \frac{1}{L_{\text{rad}}} \tag{2}$$

where L_{rad} is the radiation length, and p_0 is the nominal muon momentum. The scattering density of a material thus represents the mean square scattering angle of muons with nominal momentum passing through a unit depth of that material. Values (in mrad per centimeter) are about 3 for aluminum, 14 for iron, and 78 for uranium, for example. With the measured Δx and $\Delta \theta$, the scattering density is estimated. The definition of Δx and $\Delta \theta$ is shown in Figure 2. The detailed theory behind and steps of this algorithm are described in [7].

3. Literature review on muon imaging

3.1. Muon imaging techniques

1) University of Surrey

P. M. Jenneson, et al. from University of Surrey reported their work on imaging large vessels using cosmic-ray muon energy-loss techniques. In traditional attenuation-loss techniques, the expected flux (from a measurement when there is no sample between the detectors) is compared to the measured number of four-fold coincidence measurements, which relies on a stable intensity of horizontal muons. Alternatively, energy-loss techniques measure the energy of the

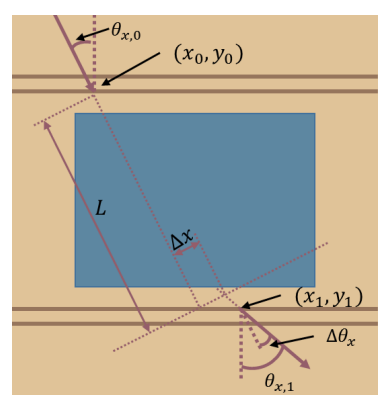


Figure 2. Two-dimensional projection of scattering and displacement used to describe multiple Coulomb scattering. In this and other figures, the magnitudes of changes are greatly exaggerated [6].

muons before and after passing through the sample. Their simulation study shows that the use of muon energy-loss techniques in imaging of large vessels is a promising solution. Relying on traditional attenuation-loss of horizontal muons, it takes years to accumulate enough statistics to see differences in various samples, while these differences can be easily discerned with muon energy-loss techniques with just a few muons [8].

2) Los Alamos National Lab

LANL has done a lot of great work on muon imaging. William C. Priedhorsky et al proposed a 3-D muon imaging technique in 2003 based on multiple scattering of cosmic ray muons, to detect and identify high-Z materials hidden inside large volumes. They developed a small-scale experimental detector system to validate their design, as shown in Figure 3. The detector stack consists of four ionizing radiation tracking chambers that measure a total of eight X and eight Y locations for each muon. The top two detectors measured the incident muon track, while the bottom two measured the track after scattering. The multiple measurements were used to resolve a directional ambiguity in drift time correction in the detectors. The position precision was about 400 mm FWHM. They were able to reconstruct a 3-D image of a tungsten cylinder using a point of closest approach (POCA) with the data collected over several hours [9]. They also did simulations of imaging large objects and produced encouraging results.

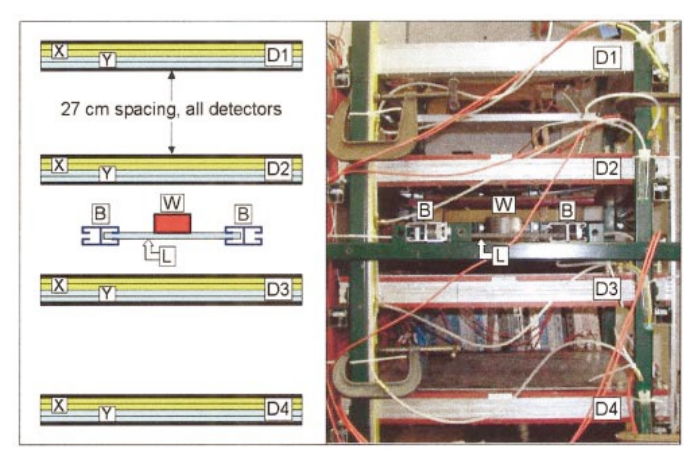


Figure 3. The experimental apparatus. Four muon detectors (D1– D4) with a 27 cm vertical spacing were used to obtain particle positions and angles in two orthogonal coordinates (X and Y). A tungsten cylinder (W, 5.5 cm radius, 35.7 cm height) was used for a test object, supported on a 1 cm thick Lexan plate (L) and steel support beams (B). [9]

Inspired by the failure of reactors at Fukushima Daiichi, John Perry et al recently proposed to image a reactor core using the multiple scattering of the near horizontal component of the muon flux. They tested their mini muon tracker (MMT) on The University of New Mexico Research Reactor (UNMRR) as shown in Figure 4 [10]. The MMT contains two supermodules (one above and one below). Each supermodule, comprised of 3 sets of x-y planes, measures the trajectories of muons passing through a region of interest. Individual drift tubes have a 5 cm outside diameter, 1.2 m length, and 0.9 mm wall thickness. They are sealed on both ends with welded aluminum end-caps [11]. Drift tubes are arranged in a stacked, dense-pack of double layers, and are able to detect interacting charged particles with high efficiency. The MMT supermodules were offset by 1.9 meters vertically and 3.81 meters horizontally during the reactor measurements. Eight hundred and ninety one hours of data collection was performed due to the low flux of muons near horizontal angles. As a result, the core with access port structures, the graphite reflector, lead shielding, and the water tank could all be observed in both the experiment and the simulation.

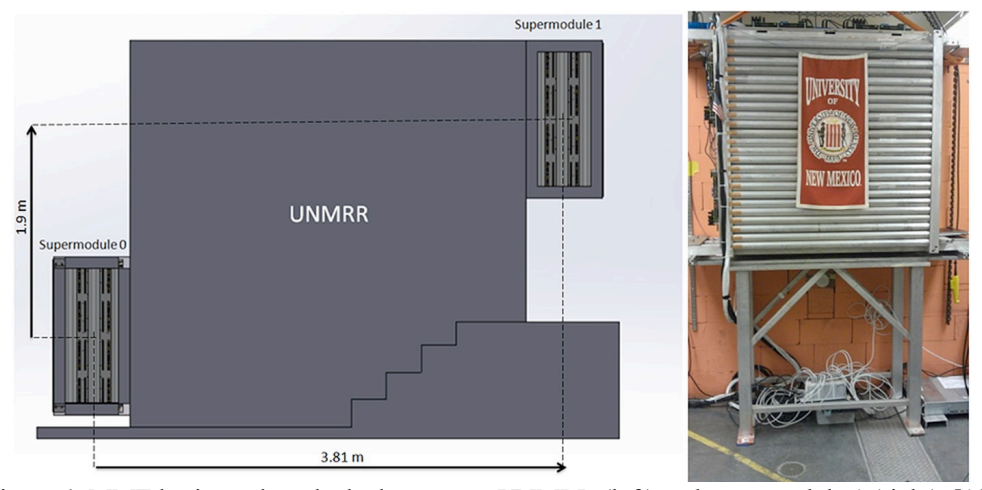


Figure 4. MMT horizontal mode deployment at UNMRR (left) and supermodule 1 (right). [10]

3) University of Glasgow

D.F. Mahon et al from University of Glasgow proposed a new type of muon tracker using scintillating fibers. This system consists of four scintillating-fiber tracker modules, two situated above and two below the volume under interrogation (the assay volume) as shown in Figure 5. Each module comprises two orthogonal planes of Saint-Gobain plastic scintillating fibers with 2 mm pitch and 97% active cross-sectional area. One detection plane contains a single layer of 128 fibers optically bonded onto low-Z, machine-grooved support sheets, providing a high spatial resolution of 2 mm. The performance of the detector was found to be stable with optimal detection efficiencies around 80% for a single layer. First results from the project have confirmed the high-Z material detection capabilities of this detector system. Discrimination between low (air), medium (stainless steel) and high Z (lead and uranium) materials was observed with several weeks of cosmic-ray muon exposure [12].

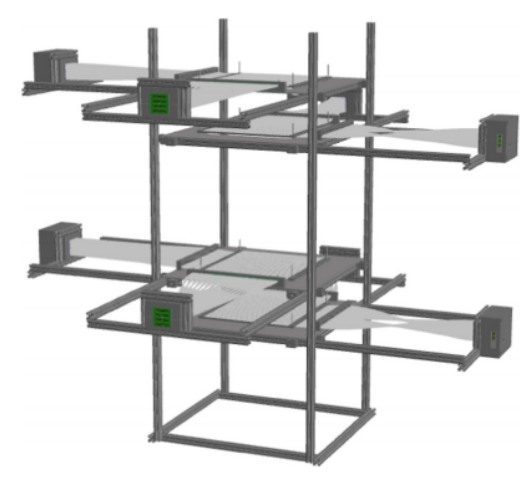


Figure 5. CAD model of the prototype Glasgow MT detector [12].

4) Korea Basic Science Institute Busan Center

H. S. Lee et al. developed a small-scale experimental system with a layer of 8 plastic scintillators. Each detector has an active area of 6 cm by 100 cm with a thickness of 2 cm. Two of them are BC408 scintillators from Bicron while the others are equivalent to BC408 from Eljin and Rexon. Two 2-inch photomultipliers (Hamamatsu, H1161 and H7195) read the scintillating light at both ends of the plastic scintillator. Each scintillator records particle tracks at two positions in each of two orthogonal coordinates. The coordinate was calculated from the product of scintillating light velocity and the time difference between recorded TDC values at both ends [13]. This is a preliminary study supporting the ability to reconstruct high-Z material objects with cosmic-ray muons using plastic scintillation detector.

5) Decision Sciences International Corporation

Decision Sciences International Corporation has commercialized technology utilizing cosmic ray background radiation for the interrogation of maritime cargo containers and other cargo conveyances for nuclear and conventional weapons of mass destruction (WMD). Their Multi-Mode Passive Detection System (MMPDS) utilizes large arrays of drift tubes above and below the volume of interest [14]. The basic idea is similar to LANL's design.

Gary Blanpied et al reported a new method to apply cosmic ray tomography in a manner that can detect and characterize not only dense objects (tungsten, lead, uranium) but also medium- and light-atomic-mass materials. Since electrons are appreciably scattered by light elements and stopped by sufficient thicknesses of materials containing medium-atomic-mass elements, combining the response of muons and electrons can extend the range of material detection and characterization beyond SNM to other types of contraband [15]. Figure 6 shows the ratio of scattering to stopping can be used for identifying the materials based on the agreement of experiment and simulation results. They demonstrate that a scanner based upon passive radiation from cosmic ray particles as well as detection of emitted gamma rays is able to detect and classify a wide range of materials in reasonable timeframes. With image segmentation and the scattered and stopped tracks one can extract the scattering, the stopping, the ratio of scattering/stopping and the gamma signal as features for classification of detected objects, which is currently being investigated.

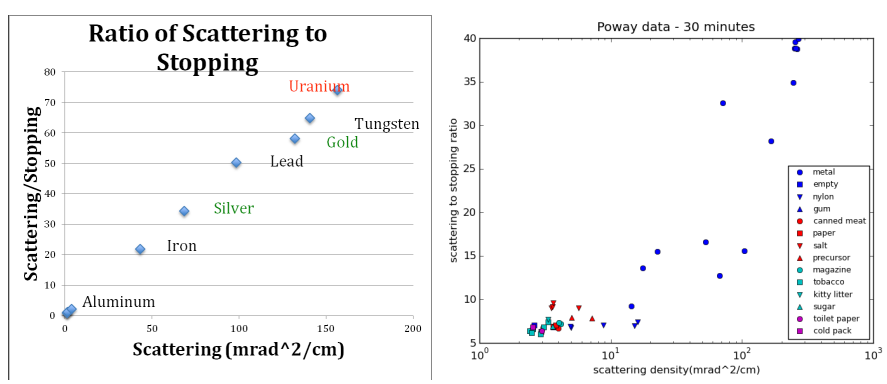


Figure 6. Ratio of scattering to stopping versus scattering from simulation (left) and experiment (right) results [15].

6) National Security Technologies, LLC

National Security Technologies, LLC proposed the Configurable Muon Tracker (CMT), shown in Figure 7, as an adaptation of the existing drift tube detector commercially available from Decision Sciences International Corporation (DSIC). They engineered the CMT around commercially available drift tube assemblies to make a detector that is more versatile than previous drift tube assemblies, as shown in Figure 7 [16]. They were able to identify a Tungsten sphere with 4930 minutes of horizontal mode imaging and 880 minutes of vertical mode imaging. A longer time is needed in horizontal mode due to the decrease in horizontal muon flux. Efforts are ongoing to improve the geometric calibration and the drift time calibration for the drift tubes. They believe the improved calibrations and the additional post processing are expected to give significant improvements to the image quality and resolution.



Figure 7. The CMT is shown set up for operation in horizontal mode (left) and vertical mode (right) [16].

7) Tsinghua University

A Tsinghua University group built the TUMUTY (Tsinghua University Muon Tomography Facility) system, which is shown in Figure 8 [17]. There are six groups of MRPC (Multi-gap resistive plate chamber) detectors, three for the incident muon track and three for the outgoing track. Each group consists of two MRPC layers to realize the x-y 2D readout. The volume for imaging is nearly $0.7 \times 0.7 \times 0.9$ m³, and the prototype is nearly 3m high in total. The multiple layer design enables the energy measurement via TOF (Time of Flight). The detector spatial resolution in TUMUTY is better than 1 mm, as a consequence, the angular resolution of the fitted muon track is about 10 mrad [18]. Baihui Yu et al proposed a Maximum a Posteriori

(MAP) algorithm with an edge preserving prior to regularize the reconstruction. A surrogate algorithm and convex function separation are employed to simplify the optimization, which transfer the MAP problem to a cubic equation. The test results show that MAP can significantly improve the image quality compared with the conventional ML reconstruction algorithm. [17].

Based on multiple Coulomb scattering and Bayesian theory, the most probable trajectory (MPT) of a muon in the materials can be analytically extracted with the known incident and scattering trajectories. Hengguan Yi et al developed a modified algorithm based on this MPT algorithm. They showed encouraging results of this image reconstruction algorithm are smoother and better contrast than the ones of the original PoCA algorithm. [19].

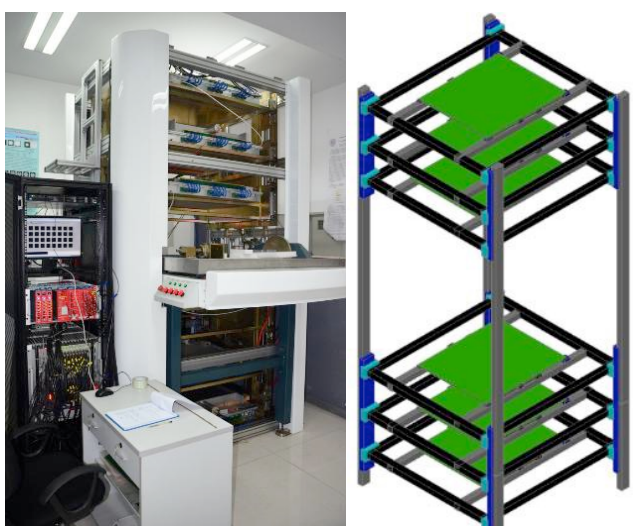


Figure 8. Recent photo and schematics of TUMUTY [17]

3.2. Muon imaging simulations

Geant4 is widely used as the Monte Carlo simulation tool to study muon tomography because it has built-in muon classes and physical processes [20, 21]. These classes use the standard GEANT4 muon physics processes for ionization, multiple scattering, Bremsstrahlung, and pair production with default settings for production thresholds of secondary particles [21]. In addition to the basic package of Geant4, the CRY Monte Carlo generator may also be used to generate muons with an angular distribution and an energy spectrum corresponding to those of cosmic ray muons at sea level. Chris Hagmann et al developed this Monte Carlo model of the Earth's atmosphere and implemented it in three different codes (Geant4, MCNPX, and FLUKA). Primary protons in the energy range of 1 GeV – 100 TeV are injected at the top of the atmosphere. The codes follow the tracks of all relevant secondary particles (neutrons, muons, gammas, electrons, and pions) and tally their fluxes at selectable altitudes. Comparisons with cosmic ray data at sea level show good agreement [22]. Figure 9 shows the MC-generated muon spectrum and data measured at sea level.

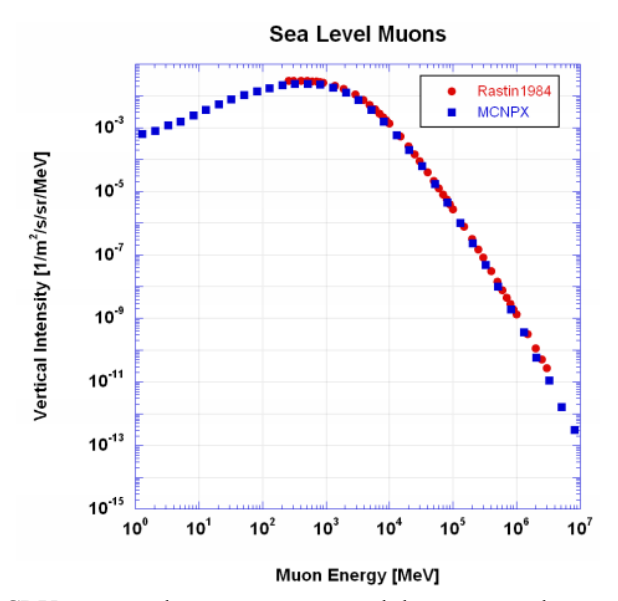


Figure 9. CRY-generated muon spectrum and data measured at sea level [22].

3.3. Muon detectors

Since the muon is a heavy charged-particle with a huge amount of energy, it deposits energy in all kinds of materials when passing through them. Thus, almost all kinds of detectors can be used to detect muons. However, some special requirements are essential for muon imaging applications. The first essential requirement of a muon detector system is coincidence timing in two or more detectors placed on each side of the item of interest to register a muon event. Second, in order to reconstruct the incident and outgoing trajectories of the muon, at least two planes of position sensitive detectors are required on each side of the container of interest. Moreover, considering that the scattering distribution is also sensitive to muon energy, the energy determination ability is also required in most designs. Finally, efficient detectors are important for cosmic ray muon detection in order to optimize statistics and, therefore, reduce the time taken to collect sufficient data [23].

Various designs have been developed to determine the position information of muons. Arrays of drift tubes are very widely used as positive-sensitive detectors of muon. Drift tubes are arranged in a stacked, dense-pack of double layers, and are able to detect interacting charged particles with high efficiency [10]. LANL, Decision Sciences International Corporation and National Security Technologies utilize drift tubes, as mentioned in Section 2.1.1. Chung Yau and Elton Ho proposed to use NaI detectors and polystyrene plastic scintillators [24]. Micro-pattern gas detectors (MPGDs), specifically GEMs are also commonly used, such as in [25]. A GEM can achieve the highest spatial resolutions (50 to 150 μm) and allows the construction of quite compact muon tracking stations of only ~10 cm thickness. The University of Glasgow proposed a muon tracker using scintillating-fiber [10]. The spatial resolution of this type of muon tracker is determined by the size of scintillating-fiber, which is 2 mm in their design. Some others also proposed to use plastic scintillators. Since plastic scintillator is our primary choice, we will elaborate on it in next section.

3.4. Plastic scintillator and light readout options

Plastic scintillators are good materials to detect muons due to their high efficiency and stability. There are different ways to extract position information from scintillators, as described below.

V. Anghel et al built their first prototype that consists of four 1.0 m² layers of scintillator strips with wavelength shifting (WLS) fibres coupled to multi-anode photo-multiplier tubes (PMTs) [26]. Then, they constructed the Cosmic Ray Inspection and Passive Tomography (CRIPT) second generation prototype. CRIPT uses 1,452 scintillator strips that are 2.0 m long so that each detector layer is 2.0 m × 2.0 m; there are 121 strips per layer. As with the first prototype, the strips are read-out by WLS fibers that are coupled to 64-anode PMTs. Two orthogonal layers of strips are required to determine the x and y coordinates of the muon's location. For this reason, each detector layer in CRIPT is actually a "super-layer" consisting of x- and y-strips. Figure 10 shows one of the super-layers during construction [27]. A precise measurement of the location of a muon in a super-layer is made by comparing the integrated charges of digitized waveforms from adjacent scintillator strips. If there are enough above-threshold hits in each layer specified in the trigger, the waveforms from all above-threshold channels are saved for analysis. The "best" hit candidate for each layer is determined and used to reconstruct muon track segments in the upper tracker and lower tracker. Figure 10 shows segments in the UT and LT, their projections into the imaging volume, and hits in the detectors in the spectrometer [27].

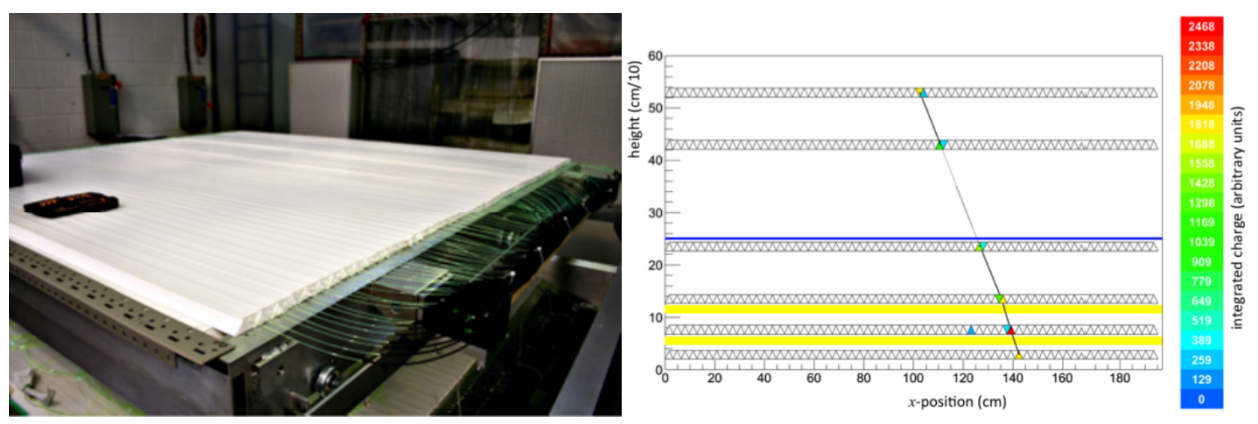


Figure 10. Single super-layer of scintillator detectors during assembly (left); Track in the CRIPT muon detectors (right). [27].

J. Dong et al proposed to use scintillator planes instead of scintillator strips. To enable a large area plastic scintillator plane to determine position, it must be divided into small tiles and the WLS fibers can be used to collect the light from each tile. The size of the plastic scintillator plane used in this paper is 32×32×2.5 cm³. Sixteen identical grooves were curved uniformly on one side of the plastic scintillator. The width of a groove is 9.5mm, and the depth is 1.1 mm. The pitch between every two grooves is 19.32mm. Second, 9 WLS fibers are placed into a single grooves. Then the 16 bunches of WLS fibers are coupled to the 16 channels of the multi-anode photomultiplier tube (MAPMT) separately. So the plastic scintillator is equivalently divided into 16 tiles in one dimension. As for the other side of the scintillator, the same procedure is done as for the former side. The only difference is that the direction of grooves on this side is perpendicular to those on the former side. With the design, they carried out an experiment to test

the position resolution. The cosmic ray test results show that the detector can completely reconstruct the position of incident particles, with a resolution as high as ~8.6mm [28].

Another similar idea is found in [29]. Though the application is for fast neutron imaging, it offers some useful information for us. The basic structure is the same as in [28], which is shown in Figure 11. They measured the position resolution for 1.25 cm in the x-direction and 0.45 cm in the y-direction with a collimated ^{90}Sr β -source. We believe the position resolution will be improved when it comes to muon interaction since muons deposit much more energy than the average beta from a ^{90}Sr , yielding more scintillation light, and position resolution improves as light collection increases.

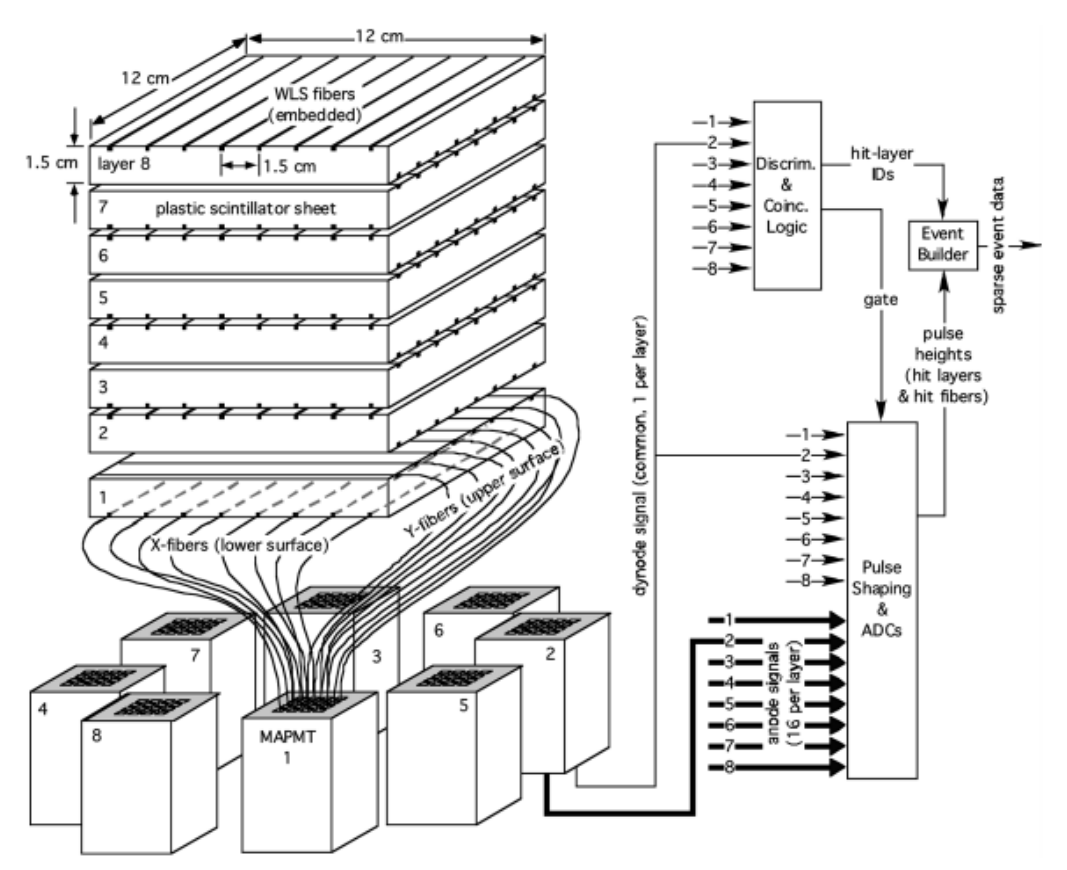


Figure 11. Conceptual design, consisting of a tower of eight position sensitive scintillator detector modules, WLS fibers (16 per module) coupled to MAPMTs and readout electronics [29].

3.5. MAPMT readout circuits

As noticed, all of the designs with plastic scintillators and WLS fibers require the readout circuits for MAPMTs. However, if one uses one ADC or QDC channel for each detector channel, the cost of instrumenting a large scale muon tomography system with MAPMTs will be prohibitive.

Fortunately, some multiplexing methods developed for positron emission tomography (PET) can be applied to muon tomography. There are generally two categories of multiplexing: light multiplexing (also known as light sharing) and charge multiplexing [30]. The former is used when the pitch of the scintillator elements is smaller than the size of photo detector elements. In

our application, it is the WLS fiber that is connected to the pixelated anode. Thus, charge multiplexing is chosen. Charge multiplexing schemes include two implementations: resistive and capacitive. A commonly used resistive multiplexing schemes for signals of a PMT, Anger logic, aims to reduce the multiple outputs of a multi-channel PMT system to just 4 using a variety of resistor networks. An example is given in [31], which is shown in Figure 12.

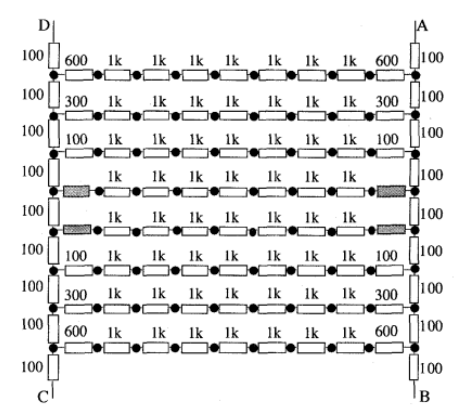


Figure 12. The resistor network. All resistor values in ohms. The gray filled resistors are 0 ohms [31].

By using the resistor network, we will be able to reduce the numbers of ADCs or QDCs in our design. However, the resistor network has its drawbacks. For example, in some design, the capability of simultaneous readout for multiple channels is required.

4. Preliminary simulation studies

4.1. Simulation study on energy deposited by muons in EJ-200 scintillators

This section describes the study of expected cosmic ray muon energy deposition in our chosen detector material. A piece of EJ-200 plastic scintillator with exactly the same size with our scintillator (32 cm by 32 cm by 2.5 cm) was modeled. To simulate the muon energy deposition in EJ-200 in our design, it was bombarded from the top with mono-directional muons with different kinetic energies in GeV range. The simulation was done with both Geant4 and MCNP6. The energy deposition for each muon event was recorded, and the distributions are shown in Figure 13 and Figure 14. As indicated by both simulation tools, the energy deposit by muon in our scintillator has a lower limit, around 3.6 MeV.

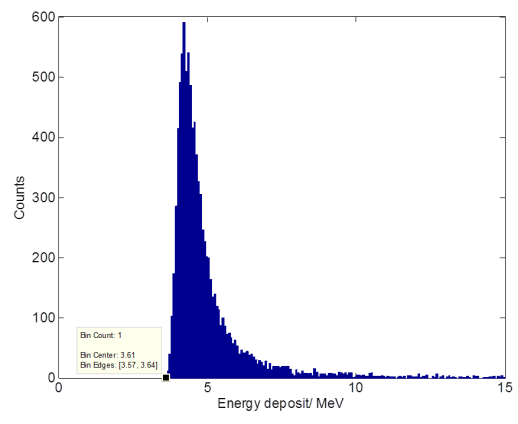


Figure 13. Geant4 simulation of energy deposit distribution by muon

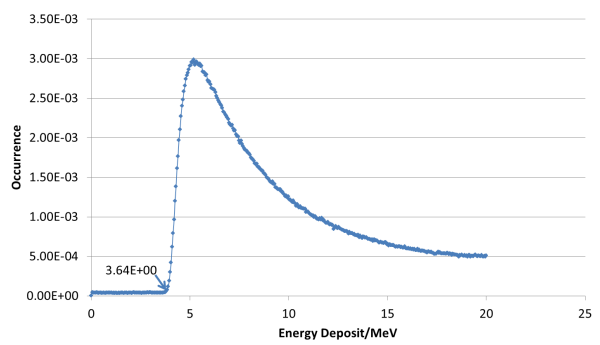


Figure 14. MCNP6 simulation of energy deposit distribution by muon

4.2. Muon imaging based on transmission – 2D

Muon radiography has been utilized previously to image large-scale objects. It has also been used to measure the depth of the overburden of a tunnel, to search for hidden chambers in a pyramid and to predict volcano eruption [8-10]. The image formed is an attenuation map of muon flux revealing the radiation length traveled by muons before entering the detectors, which indicates the thickness of the object.

To study the muon radiography, a 1:1 model of a generic DSC was created in Geant4. The top view and 3D view of this model generated by Geant4 visualization tool are shown in Figure 15. The outer radius of the gamma shielding ring is 120.1 cm, which is marked as blue in the top view. The size of a fuel assembly is 22.9 cm. One out of twenty-four used fuel assemblies was removed intentionally to test the detection capability of this imaging method. The position of the missing assembly is [-11.45 cm, -11.45 cm]. The muon source was modeled as a uniform plane source located above the cask, emitting 4 GeV monoenergetic muons with an angular distribution that is peaked at the zenith and falls off as $\cos^2\theta$. All the most significant particle types were declared in the simulations, but the less significant interactions like muon capture and

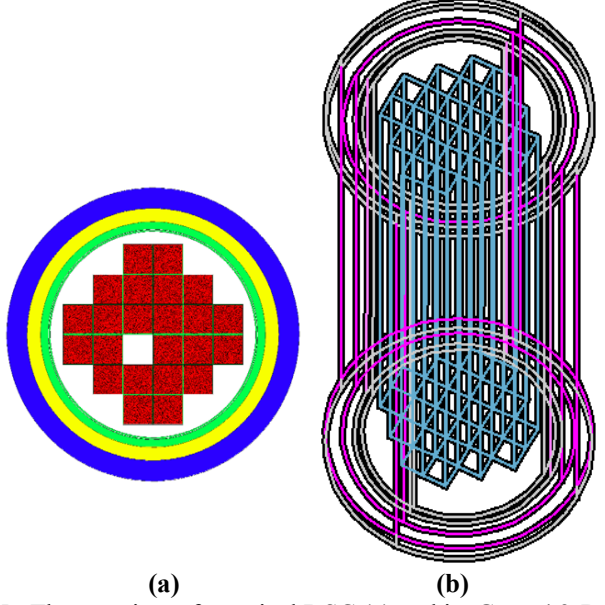


Figure 15. The top view of a typical DSC (a) and its Geant4 3-D model (b)

muon decay in-flight were neglected. Specifically for muons, multiple scattering, ionization, bremsstrahlung and pair production were included in the simulation physics. For the purpose of this work, the detector geometry is generic and was simplified as an ideal position-sensitive detection plane placed underneath the cask, recording the positions of transmitted muons as they cross the detection plane. Also, the trackers were made insensitive to other particles.

The image was reconstructed from a 2D histogram of muon counts measured on the detection plane underneath the cask, forming a "projection" of the cask. The reconstructed image is shown in Figure 16 (a). The pixel size used in the 2D-histogram is 4 cm by 4 cm. From the image, one can observe the large attenuation caused by high-Z material residing inside the fuel assemblies, so the basic shape of the fuel assemblies as well as the lead shielding ring can be recognized. One can also locate the missing assembly by examining a slice of the 2D histogram at the near position of it, as shown in Figure 16 (b). However, the image quality was so poor and no inside information is obtained. Moreover, if the fuel assemblies were not placed orderly, this method would be much less applicable. Also, to make a detector as an even bigger size than the diameter of a DSC is extremely expensive and difficult.

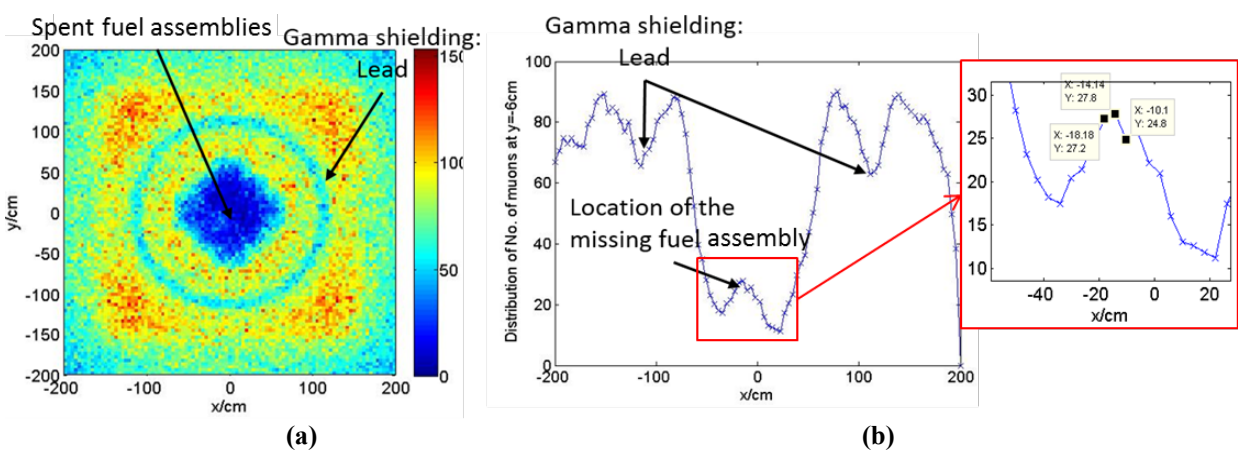


Figure 16. (a) The reconstructed image based on muon "projection" (b) The cross-sectional curve showing the missing assembly

4.3. Muon imaging based on scattering – 3D

Muon tomography was developed as an extension of the concept of muon attenuation radiography. In muon tomography, the incoming and outgoing directions are tracked for each muon. The spread of the deflection angle of scattered muons provides a way to distinguish high-Z materials in the volume of interest. In this section, modeling and reconstruction of 3D images using two well-known algorithms is studied.

4.3.1. Modeling of simple geometries with POCA

To start with, three letters built with bricks were modeled to study the basic idea of 3D muon tomography. The geometry is shown in Figure 17(a). The letters are made of bricks with three different materials. All the bricks are in the same size, which are 40" by 15" by 15". The same muon source and the selection of the physics processes as described in Section 2.4 were used in this simulation. The detector was simplified as two perfect position-sensitive detection planes

placed above and below the letters as the incident and outgoing muon trackers, recording the positions and directions of transmitted muons as they cross the volume of interest.

The point of closest approach (POCA) algorithm was implemented for the reconstruction of simulated data. The POCA algorithm ignores multiple coulomb scattering, instead assuming that a muon scattered at a single point [7]. Based on the direction and position information on both the incident side and outgoing side, the scattering point and the scattering angle are evaluated using POCA for each muon event. The 10 m × 4 m × 2 m whole volume was then divided into $50 \times 25 \times 25$ cells. The muon events were assigned to their voxels based on their scattering location. The standard deviation of scattering angles was then calculated for each voxel. After all these calculations, an image was reconstructed as a color map in which different colors are used to show different values of standard deviation of the scattering angle. As discussed above, the standard deviation of the scattering angle results from the difference in radiation length, which is determined by the atomic number and density of materials. A reconstructed 3D image is shown in Figure 17 (b). The result showed excellent spatial resolution as well as the ability to distinguish high-Z and low-Z materials.

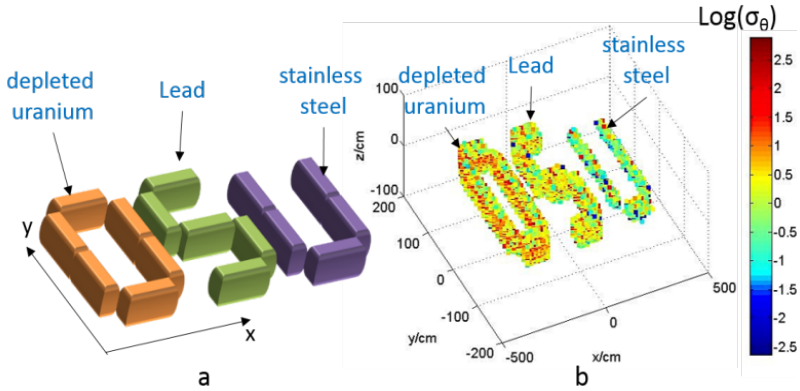


Figure 17. (a) The layout of the letter shape bricks and (b) the reconstructed image using POCA algorithm.

4.3.2. Modeling of a simplified DSC

A simulation study for imaging dry cask was also performed. The same layout of a dry cask shown in Figure 12 was used in this simulation. However, considering the dimension of our muon tomography system, the size of the dry cask was scaled down to 20 cm by 20 cm, and the fuel was simplified to a 10 cm by 10 cm by 10 cm cube. The sizes of other components (shielding) were reduced accordingly. Both POCA and ML/EM algorithms were used for image reconstruction. The reconstructed images are shown in Figure 18. The high-Z fuel block and the lead shielding are clearly observed using both algorithms. The reconstructed image using ML/EM presents less blurry edges than those reconstructed using POCA; thus, ML/EM reconstruction results in better spatial resolution.

4.4. Modeling detailed DSC

In muon tomography, the incoming and outgoing directions are tracked for each muon. Conventionally, in the vertical orientation, objects are placed between the upper and lower tracker sets. However, in our case it is hard to place any detectors underneath a DSC. Therefore,

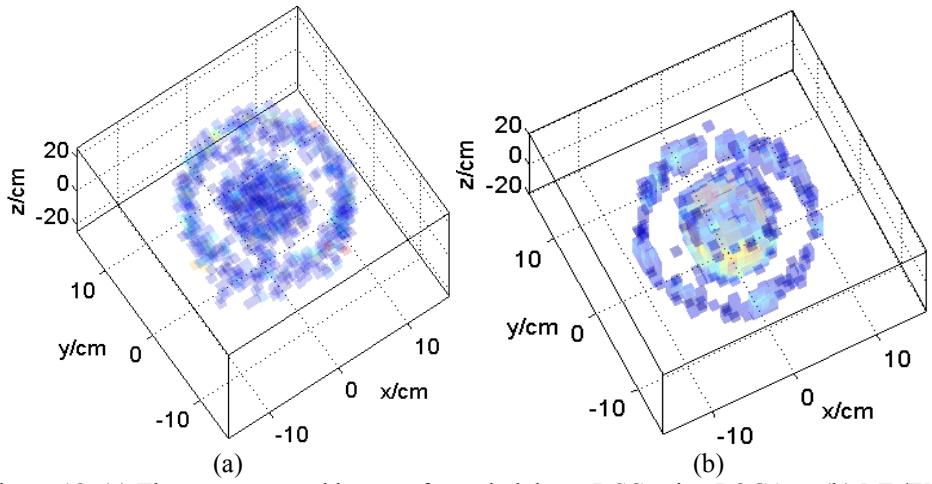


Figure 18. (a) The reconstructed image of a scaled down DSC using POCA or (b) ML/EM.

some alternative designs are considered and studied. Specifically, we modeled the Westinghouse MC-10 DSC, which is shown in Figure 19. The exact dimensions and material properties were modeled. Also, in this section, we modeled the muon trackers with the same size as the LANL MMT (Mini Muon Tracker). Figure 19 also shows the orientation of detectors. The muon source was modeled as a uniform plane source located above the cask, emitting 4 GeV monoenergetic muons with an angular distribution that is peaked at the zenith and falls off as $\cos^2\theta$. All the most significant particle types were declared in the simulations, but the less significant interactions like muon capture and muon decay in-flight were neglected. Specifically for muons, multiple scattering, ionization, bremsstrahlung and pair production were included in the simulation physics. During the simulation, 10^9 muons were generated, and only the muons that passed both detector planes were recorded.

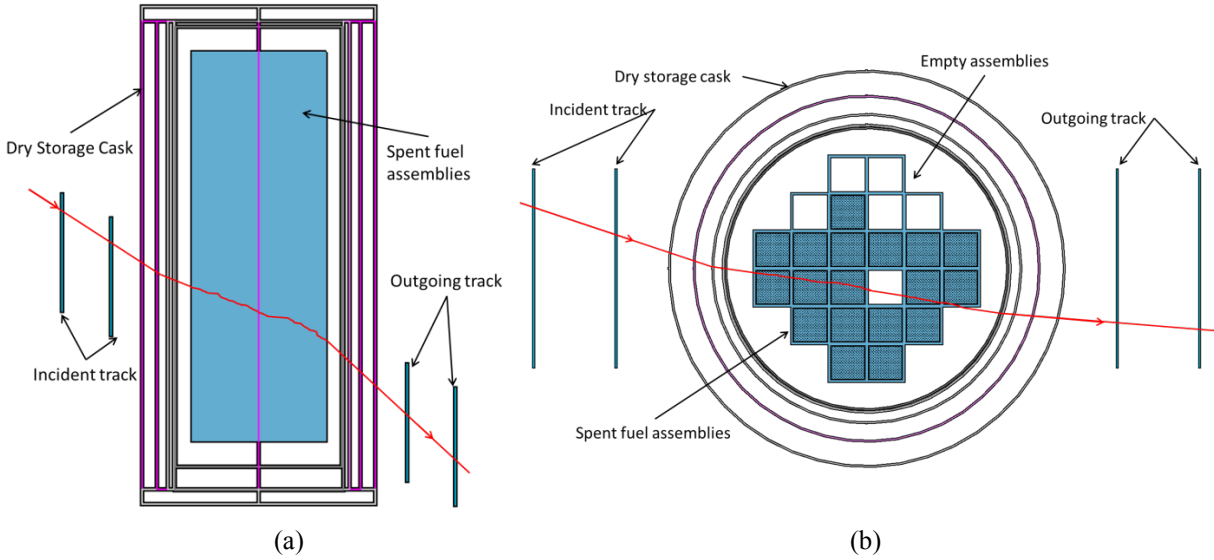


Figure 19. The side view (a) and top view (b) of the detector and DSC showing the detector orientation and the DSC content.

The point of closest approach (POCA) algorithm was implemented for the reconstruction of simulated data. Based on the direction and position information on both the incident track and

outgoing track, the scattering point is estimated as the midpoint of the line segment between the closest points on the two straight lines. After calculating the POCA, a 2-D histogram of the y and z positions of all the scattering points was taken as the reconstructed cross-sectional image of the DSC. The y-z plot of the reconstructed images is shown in Figure 20 (b). The outline shape of the fuel assemblies can be told as a whole piece. However, the scattering events at the inner part have higher probabilities to be registered. This is due to the bias brought by the geometry. To eliminate the influence of the bias and understand the image better, we modeled the same DSC with no missing assemblies. The image is shown in Figure 20 (a). Figure 20 (c) shows a subtraction of Figure 20 (b) from Figure 20 (a). From the subtraction image, it becomes possible to locate the missing assemblies. Moreover, since the difference mainly lies on y-axis, we added the values along z-axis. Figure 21 shows the total number of scattering points vs y position. Before generate this plot, we rejected the events with small scattering angle. The threshold value of the cosine of the scattering angle was chosen as 0.9900 for best performance. From this figure, it is easy to find the position of the missing assemblies.

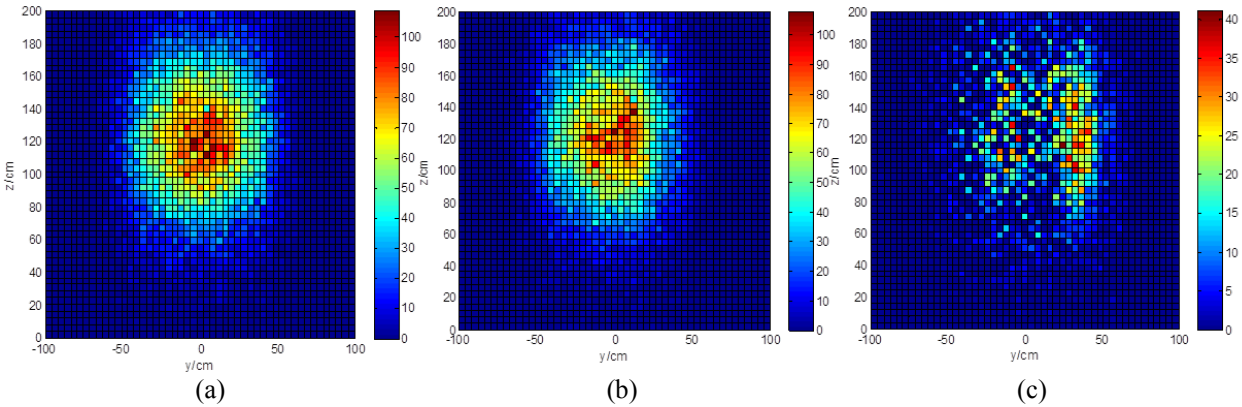


Figure 20. (a) y-z 2D histogram of the POCA scattering points from the DSC with full assemblies (b) y-z 2D histogram of the POCA scattering points from the DSC with missing assemblies (c) image subtraction

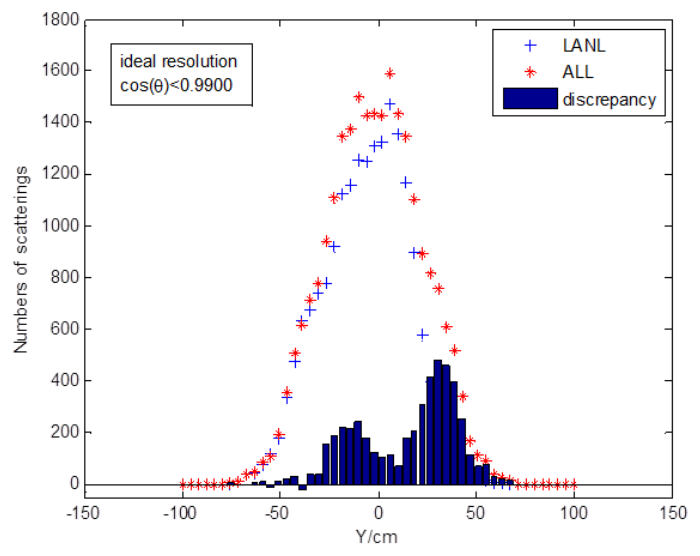


Figure 21. Total number of scattering points vs y position

In the above part, we assumed perfect position resolution of the muon detectors. However, our detectors are not able to offer a position resolution better than 1 cm. Thus, we re-evaluated the images when we assume the position resolution of the detector to be 1 cm. The same processes are done. Figure 22 and Figure 23 show the result. Here we used a larger threshold of $\cos(\theta)$, because the distribution of the scattering angle are broadened due to the induced position error when the position resolution is degraded. Although it is harder to locate the missing assemblies from the subtraction image, it is still possible to identify and locate them in the integrated image (Figure 23).

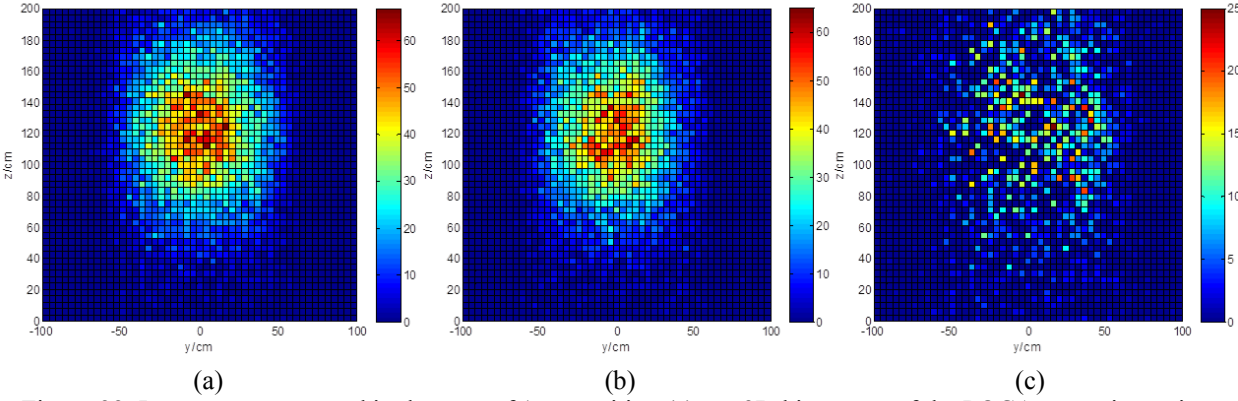


Figure 22. Images reconstructed in the case of 1cm position (a) y-z 2D histogram of the POCA scattering points from the DSC with full assemblies (b) y-z 2D histogram of the POCA scattering points from the DSC with missing assemblies (c) image subtraction.

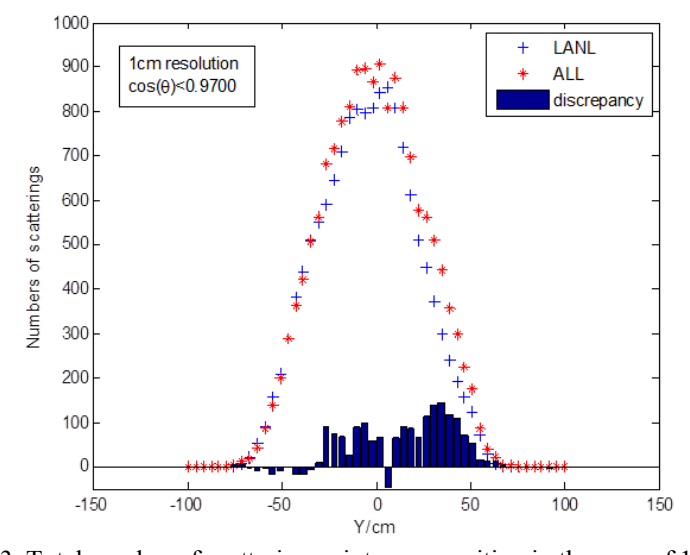


Figure 23. Total number of scattering points vs y position in the case of 1cm position

5. System design and characterization

Since the muon is a heavy charged-particle with a huge amount of energy, it deposits energy in all kinds of materials when passing through them. Thus, almost all kinds of detectors can be used to detect muons. However, some special requirements are essential for muon imaging applications. The first essential requirement of a muon detector system is coincidence timing in two or more detectors placed on each side of the item of interest to register a muon event.

Second, in order to reconstruct the incident and outgoing trajectories of the muon, at least two planes of position sensitive detectors are required on each side of the container of interest. Moreover, considering that the scattering distribution is also sensitive to muon energy, the energy determination ability is also required in most designs. Finally, efficient detectors are important for cosmic ray muon detection in order to optimize statistics and, therefore, reduce the time taken to collect sufficient data.

5.1. System design v1

In our first version of design, the position sensitive detector is based on a single-layer plastic scintillator panel in the size of 32 by 32 by 2.5 cm. 32 parallel grooves, with a pitch of 1 cm, with 2 mm width and 4 mm depth are carved on the top and bottom sides of the scintillator panel. The directions of the grooves on the top and bottom sides are perpendicular to each other. Bundles of two wavelength shifting (WLS) optical fibers are embedded in each groove for light transfer. The WLS fibers are routed to individual pixels of a 64-pixel MAPMT. The WLS fibers absorbed a portion of the scintillation light generated within the plastic scintillator by muon interactions and emit light with a different wavelength spectrum. Claddings surrounding the WLS fibers trap the light emission inside the fibers and transfer it to the MAPMT pixels for readout. Figure 25 is the Schematic drawing and the picture of the scintillator plane embedded with fibers.

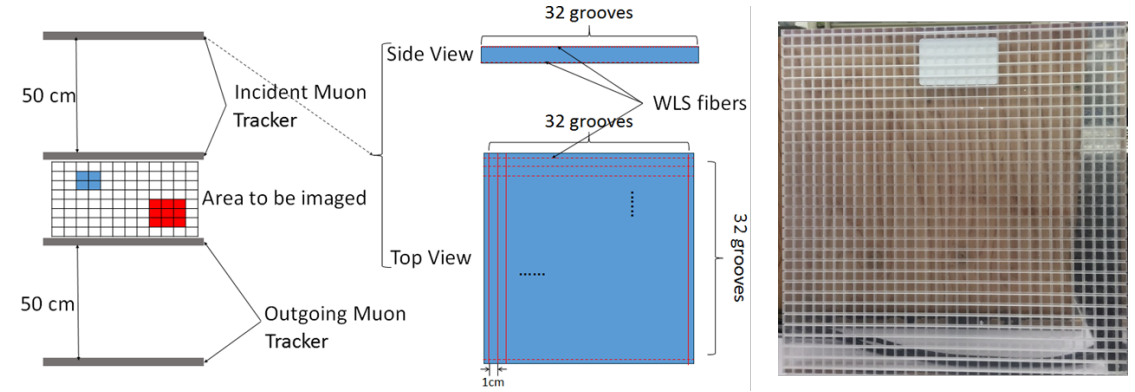


Figure 24. The schematic drawing of the first detector design using plastic scintillator planes

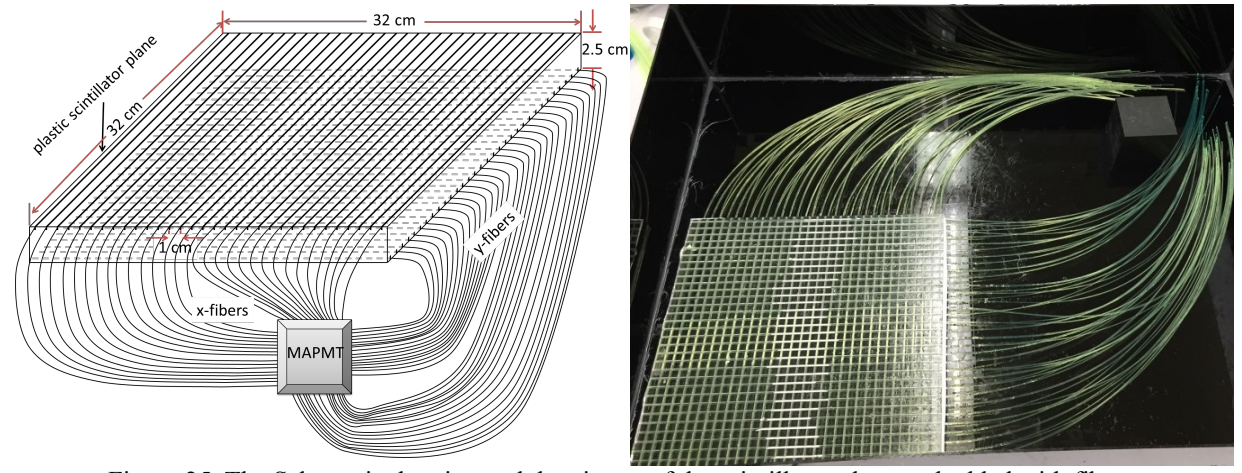


Figure 25. The Schematic drawing and the picture of the scintillator plane embedded with fibers.

The position information in one direction can be obtained from the distribution of the amplitudes from the corresponding 32 channels. As illustrated in Figure 2, when a scintillation event occurs at certain location, the light intensities, which are proportional to the signal amplitudes, of the fibers near the location follow a quasi-Gaussian distribution centered at the scintillation event. Therefore, an interpolation of the 32 amplitudes could reveal the origin of the scintillation light in each direction. By doing this, the position resolution around 1 cm is theoretically achievable.

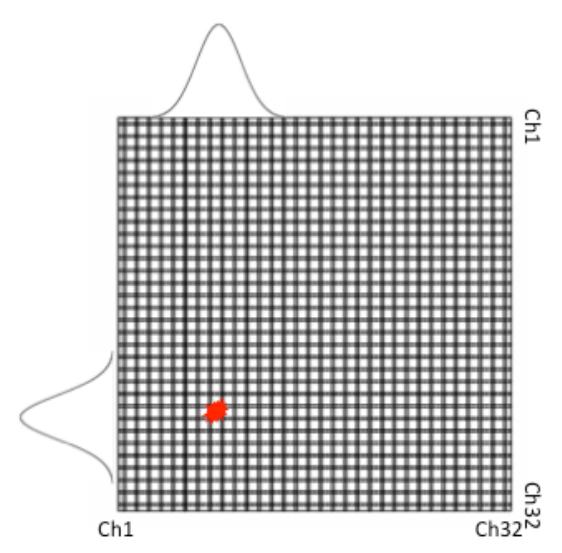


Figure 26. The concept of the position-sensitive scintillator design

Based on the well-known idea of Anger logic used to determine the positions of events, a simple 1-D resistive 'network' is introduced. In this circuit, 33 identical resistors are connected in series to form a 32-channel network for each direction. For a single channel input, the resistor network serves like a voltage divider. The relative ratio of signals from the two ends of the circuit, which are marked as A and B for the x direction and C and D for the y direction, has a linear relationship with the channel number. Specifically, the relationship is expressed as:

$$x \propto x_{ratio} = \frac{A}{A+B}; \ y \propto y_{ratio} = \frac{C}{C+D}$$
 (3)

For multiple channel inputs, the total ratio represents the weighted average ratio of each channel, where the weight is the amplitude of each channel, because the resistor network is a linear system. As introduced in the detector concept, the signal amplitudes of the fibers near the scintillation location follow a quasi-Gaussian distribution centered at the original of scintillation event. Therefore, the resistor network is performing an amplitude-weighted average on all these channels, resulting in a linear relationship of the ratio and the interaction position. The 2-D position can be estimated by measuring the signal of port A, B, C and D. The estimated position is continuous instead of being discrete as in the situation of regular multiplexing circuit. Figure 27 shows the circuit schematic for the x direction. The signals from two ends are amplified with operation amplifiers.

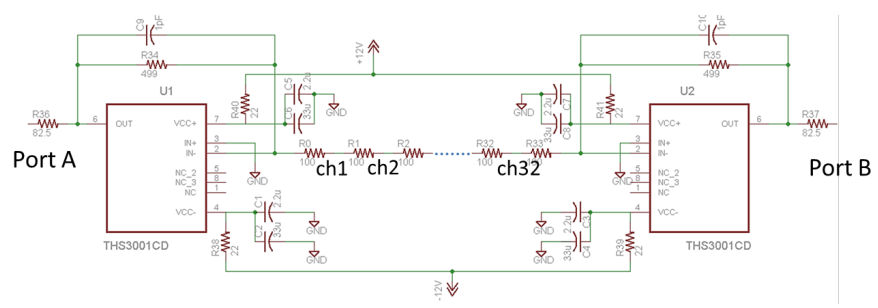


Figure 27. The schematic of the resistive network with preamplifiers for our 32-channel readout.

For a better electronic condition, PCB boards are made for the readout circuits. In this design, we design the readout circuits for two dimensions (x and y direction) in one scintillator plane on the same board to couple directly to one H8500c MAPMT. Figure 28 shows the picture of one PCB board.

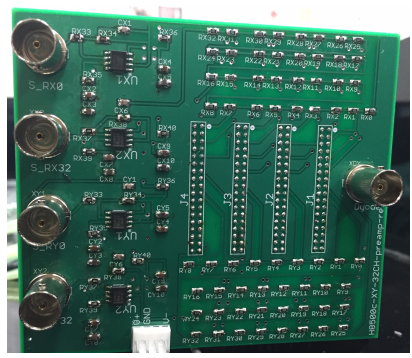


Figure 28. the picture of one PCB board for one H8500c MAPMT

The PVT-based EJ-200 by Eljen was chosen as the scintillator material. The short decay time and good temperature feature make this scintillator the perfect material for various field applications. The Saint-Gobain BCF-92 was chosen as WLS optical fibers. The BCF-92 fibers absorb blue light and emits green light. The scintillation spectrum of EJ-200 matches the absorption spectrum of the BCF-92 WLS fibers nicely, as show in Figure 29 [14, 15]. The H8500C 64-pixel MAPMT by Hamamatsu has been identified as the light sensor because of its compact design and multichannel readout capability. The H8500C has 15% quantum efficiency in green range, compared to its maximum quantum efficiency of 30%, thus a good choice for reading lights from BCF-92. The MAPMT outputs an independent anode signal for each pixel and one dynode signal shared by all the 64 pixels.

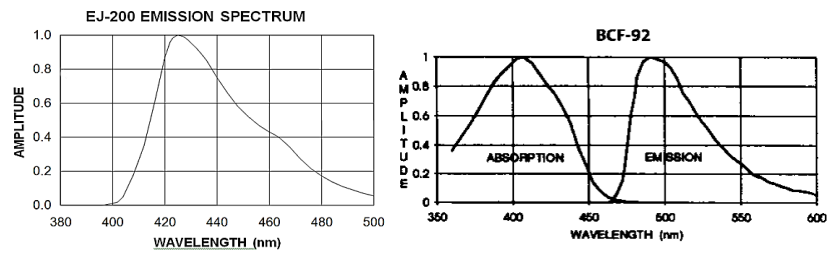


Figure 29. The emission spectrum of EJ-200¹; the absorption and emission spectra of BCF-92²

¹ http://www.eljentechnology.com/products/plastic-scintillators/ej-200-ej-204-ej-208-ej-212

² https://www.crystals.saint-gobain.com/sites/imdf.crystals.com/files/documents/sgc-scintillation-fiber_0.pdf

The fibers are square-shaped with a diameter of 1 mm. A bundle of two fibers is embedded in each groove on the scintillator surface and routed to one MAPMT pixel. Each fiber bundle was cut to the desired length and carefully polished with fine sand papers on both ends. The fibers were glued into the grooves with Eljen EJ-500 optical cement. The optical cement provides more than 95% transmission for light with wavelength of 400 nm and above. A 3-D printed module was designed for coupling the fibers and MAPMT, as seen in Figure 30. Eljen EJ-550 optical grease was applied on the window of the MAPMT to increase light transmission. The opposite ends of the fibers were trimmed to align with the edges of the scintillators. Finally, the whole scintillator was wrapped with aluminum foil to improve light collection. The aluminum also reflects some light at the other end of the fiber to improve the light collection. Figure 30 is a picture of the scintillator panel embedded with fibers, as well as the MAPMT and the coupler. A dark box made of black opaque acrylic plastic sheets is built for housing all the essential parts components of the detector system. The MAPMT is biased at 1000 V by a desktop HV power supply module, CAEN DT5521E.

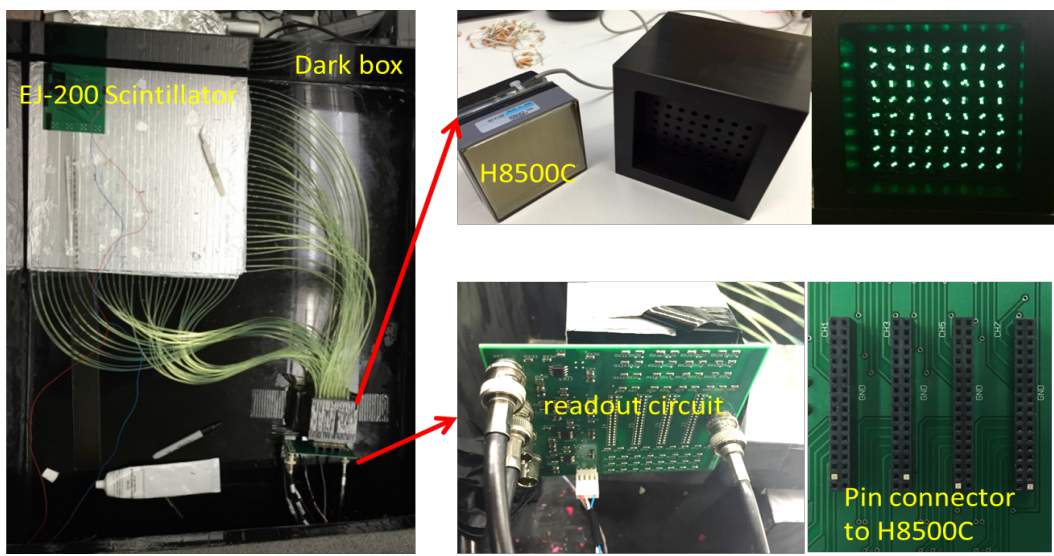


Figure 30. the experimental setup

5.1.1. Position calibration of position-sensitive detector v1

The relationship between position and signal ratio has to be established for each detector. Due to the fact that the interaction position of a gamma-ray or a neutron in a scintillator is unpredictable, using a radiation source without good collimation is not feasible for position calibration. Instead, a blue LED was used to simulate the scintillation light since the emission spectrum of EJ-200 scintillator mainly covers the blue range. Small holes on the aluminum foil were made at different locations to let the LED light in. The LED was powered by a function generator to simulate a short "scintillation" pulse. The function generator was set to generate 100 ns wide square pulses. The LED light was then expected to be absorbed by the WLS fibers and transferred to the MAPMT. The signals from the MAPMAT were acquired using a DSO-X3104A oscilloscope, which has a maximum sampling rate of 5 GSPS and a resolution of 8-bits. The used dynamic range was 5V. In the following study, pulses were acquired at 1GSPs in a 2.5 µs window and processed offline in MATLAB on a PC.

The test was done at 63 different locations across the detector panel. The center of the scintillator was set to be [0, 0]. Figure 31 shows the distribution of the measurement points. At each position, 5000 events were acquired. For each event, signals from all the four channels (two in the x direction and two in the y direction), marked as A, B, C and D, were acquired. Figure 32 shows an example of the set of signals from one event.

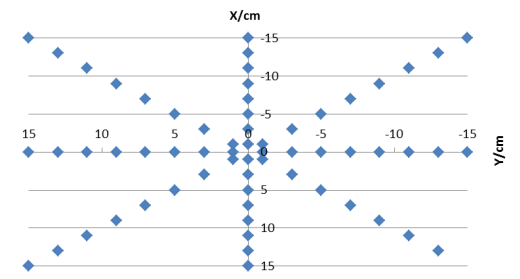


Figure 31. The positions of the 63 tested points

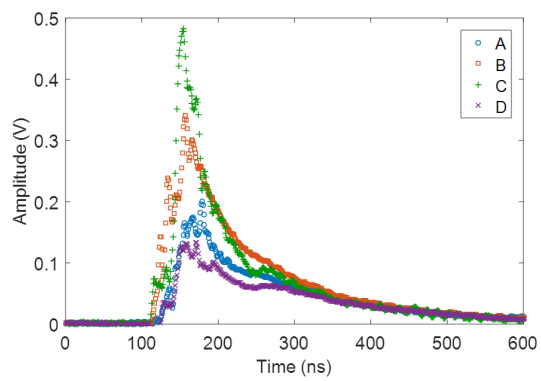


Figure 32. The example of a set of A, B, C and D signals.

The data processing was performed for each individual tested position with Matlab. In each set of data, the amplitudes of A, B, C and D are simply calculated as the integrals of the pulses. Then the x_ratio and the y_ratio are calculated using eq. 3. The calculated x_ratio and y_ratio are both fitted with Gaussian distribution. Figure 33 shows an example of the fitting process at position [-1, -1]. Figure 34 is the plot of the mean x_ratio vs. the mean y_ratio. The error bars in the plot shows the Gaussian standard deviation of each ratio. This scatter plot has a similar shape as Figure 31, which demonstrates the relationship between the position and the ratio.

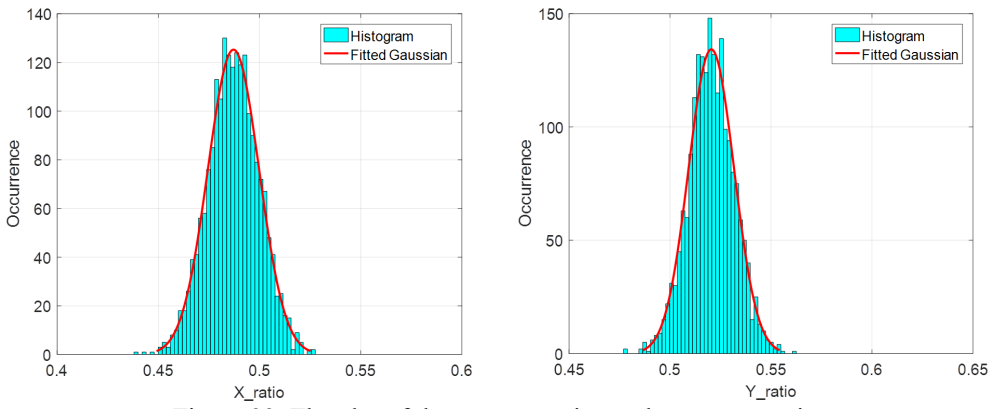


Figure 33. The plot of the mean x ratio vs. the mean y ratio

The position-ratio relationship was then quantified independently for x and y directions. Ideally, ratio_x and x are linearly dependent, and so for ratio_y and y. However, the ratio, which is dependent on the distribution of signal amplitude from adjacent fibers, largely relies on the reflection of scintillation light. Therefore, when the position is close to the edge of the scintillators, the light reflection and absorption becomes more complicated. In this case, the linearity is distorted when position approaches the scintillator edges. Therefore, instead of using linear regression to fit the relation between the ratio and position, we used a 6th order polynomial regression. Figure 35 shows the result of relationship between the ratio and position. This calibration process is done individually for all four detectors. Figure 36 is the linear regression of the relationship of x from -13 cm to 13 cm

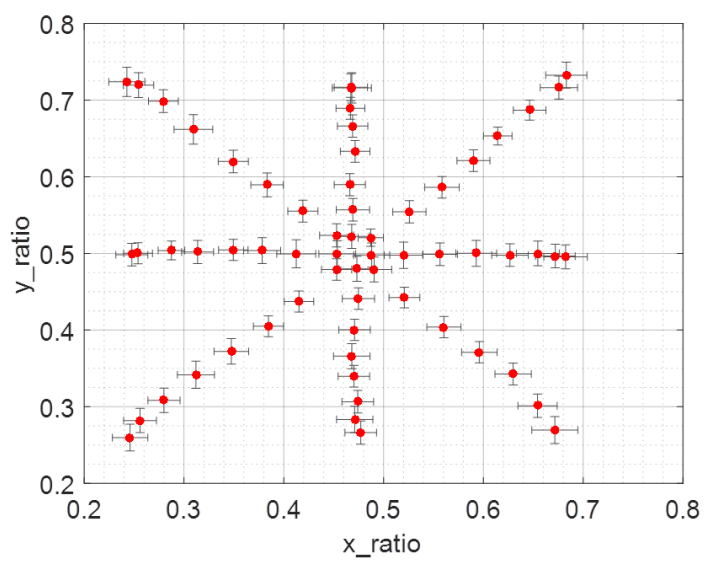


Figure 34. The plot of the mean x ratio vs. the mean y ratio

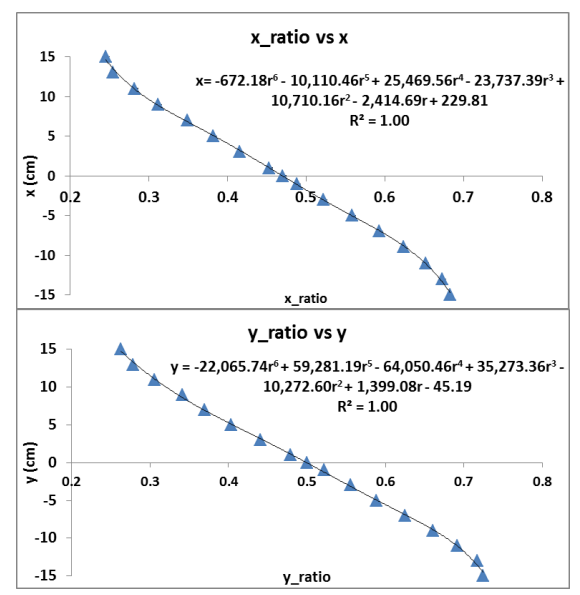


Figure 35. The plot of the mean x_ratio vs. x and the fitted curve and function; the plot of the mean y_ratio vs. y. and the fitted curve and function.

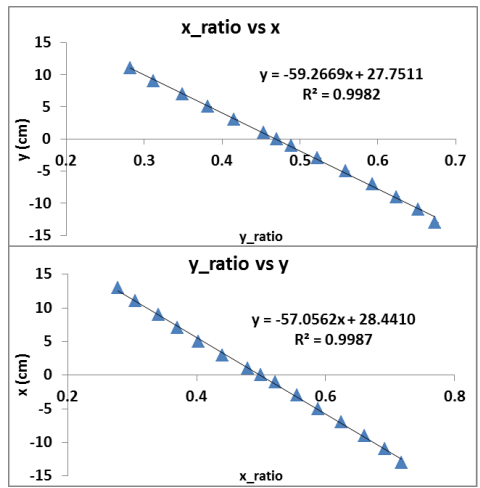


Figure 36. The linear fitted line of the mean x_ratio vs. x for x from -13 cm to 13 cm; the linear fitted line of the mean y ratio vs. y for y from -13 cm to 13 cm.

The calibration established the relationship between the interaction position and the output signals. The relationship can be described as a sextic polynomial equation if the edge points are considered. Alternatively, the relationship can be described as linear equation if only the inner points are taken into account. Good linearity are observed for both x (R^2 =0.9982) and y (R^2 =0.9987) direction in the range of -13 cm to 13 cm. However, this is not optimal. The imperfection of the linearity is explained in the following aspects:

- 1) The anode uniformity of the H8500c MAPMT;
- 2) The subtle difference in fiber coupling property of each channel;
- 3) The error of the position of each hole for LED light to travel into scintillator.

The anode uniformity map is usually given in the document that comes with the MAPMT. It is a map of output amplitude of each pixel when exposed to the same level of DC light. As introduced in section 2.4, the total ratio for multiple inputs at the resistor network is equivalent to the average ratio weighted by the signal amplitudes. Due to the anode uniformity, the weights, i.e. the anode amplitudes, are not exactly proportional to the total amount of light collected by the WLS fibers. This results in a distorted linearity between the position and ratio.

Moreover, the detector assembling process is not standardized, so the subtle differences could result in different light absorption and transfer properties. For instance, the lengths and the bending angles of the fibers are different from each other, leading to different light attenuation due to fiber length and fiber bending. And the possible air bubbles between the scintillator and certain fibers reduce the light being absorbed and transferred. Also, it is undesired but possible that fiber and PMT coupling are not guaranteed to be ideal.

Furthermore, the calibration is performed with a LED powered by a function generator. The LED is introduced into the scintillator through holes one the aluminum foil. The position of the holes are measured with a caliper and made with a knife manually. Thus, artificial error of the tested position is inevitable.

The position resolution of the detector design is another critical feature. As discussed in the detector concept section, the position resolution is expected to be around 1 cm. Using the standard error of the ratio at each position, the position resolution can be calculated based on the quantitative relationship between the position and the ratio. Figure 37 shows the plot of the calculated position resolution vs position. The mean position resolution in x direction for all range is 1.4030 cm, and the mean position resolution in x direction for all range is 1.1283 cm. The mean position resolution in x direction from -9 cm to 9 cm is 0.9863 cm, and the mean position resolution in y direction from -9 cm to 9 cm is 0.8253 cm.

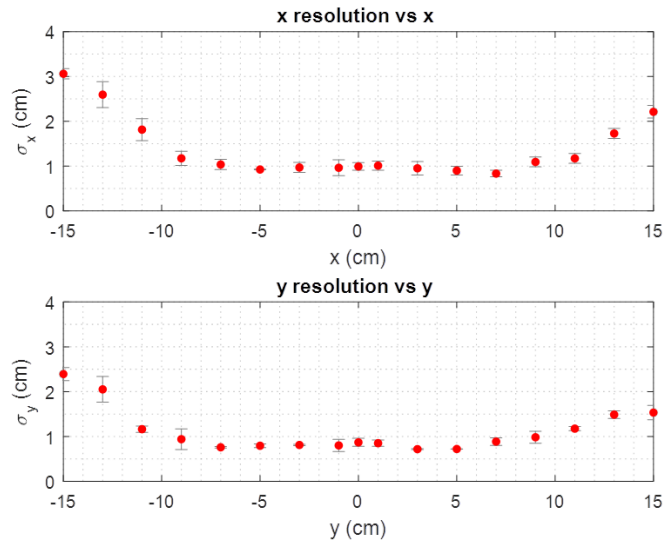


Figure 37. The plot of position resolution vs position.

However, as observed in the plot, the resolution becomes worse when the position is close to the edge of the scintillators. Two major reasons contribute to this situation. First, taking x direction as an example, either signal A or signal B has small amplitude that decreases the signal-to-noise ratio (SNR). In this case, the resolution of the ratio is degraded due to the smaller SNR. Second, the light reflection and absorption becomes more complicated at the edges, which is also the reason of the linearity distortion.

5.1.2. Integration test of v1

After assembling and calibrating all four muon detectors, the whole muon tomography system was set up as shown in Figure 38. The signal chain is illustrated in Figure 39. The signal chain mainly consists of two paths: the triggering and digitizing paths. After the signal pre-processing board, each detector has four output signals that contain the muon information and one dynode signal used to generate trigger for data acquisition. The total 16 output signals are directly connected to the input of the CAEN VX1742 32-channel Digitizer. Only the first 16 channels are used. The four dynode signals are connected to the CAEN N605 4-channel constant-fraction Discriminator. When a signal gets beyond the threshold, the discriminator produces a trigger output. Two N108 dual delay units are used to compensate the time difference brought by muon travelling. Then four outputs from the discriminator are fed into the V967B coincidence module. When a "real" muon hits all four detectors, a coincidence trigger is generated. The coincidence trigger is used as the trigger of the digitizer.

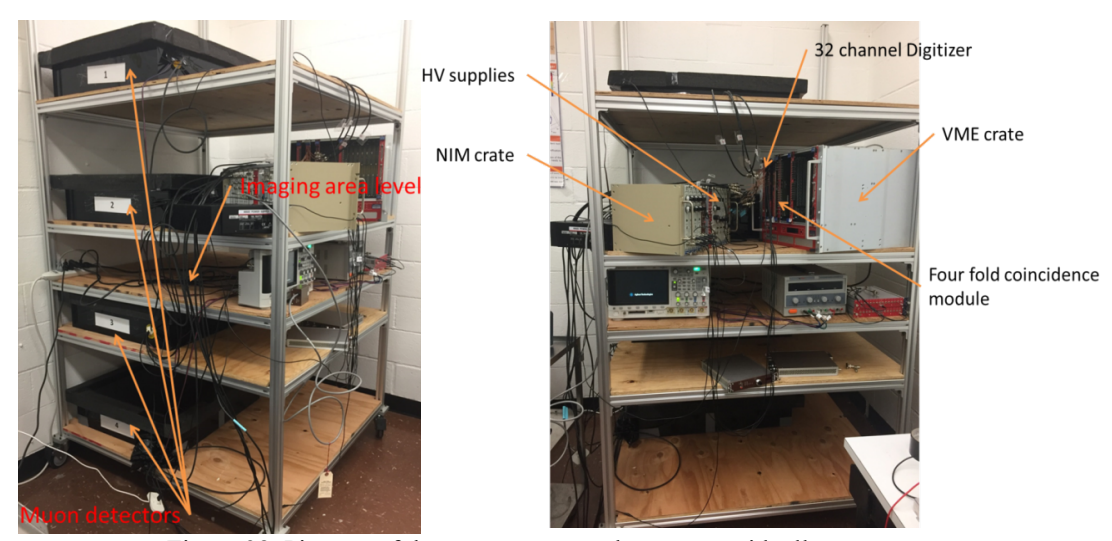


Figure 38. Pictures of the muon tomography system with all components.

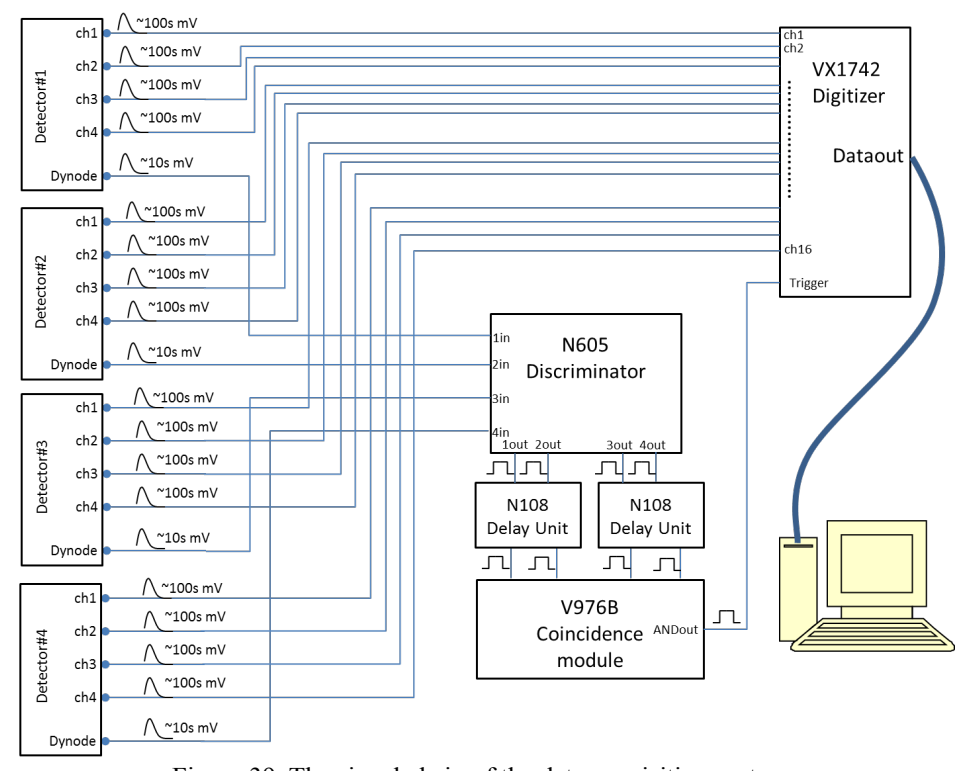


Figure 39. The signal chain of the data acquisition system.

The initial test of the whole system is done with the above system setup. The first test was run with no imaging objects. Ideally, the four measured muon positions on the four detectors should form a straight line when a muon event is detected by all detectors, because no significant scattering happened along the trajectories.

For each registered muon events, total of 16 channels of signals are acquired. Using the digitized output signals and the position calibration results from last quarterly report, the positions can be

calculated, individually for four detectors. Figure 40 shows an example of the detected muon trajectory. The four positions form a straight line as expected. The corresponding detector output signals used to extract the position information are also shown in this figure.

However, some bad examples are also observed. A bad example is shown in Figure 41. The four points are not in a straight line. Some points are even out of the boundaries of the detector. Looking at the output signals, we observed some large distortions, which are possibly brought in by the signal processing PCB board. These distortions can lead to the loss of the amplitude information and therefore the loss of the position information. It might be one of the reasons. Moreover, the position calibration is not perfect. The factor will be examined after the signal distortion problem is resolved.

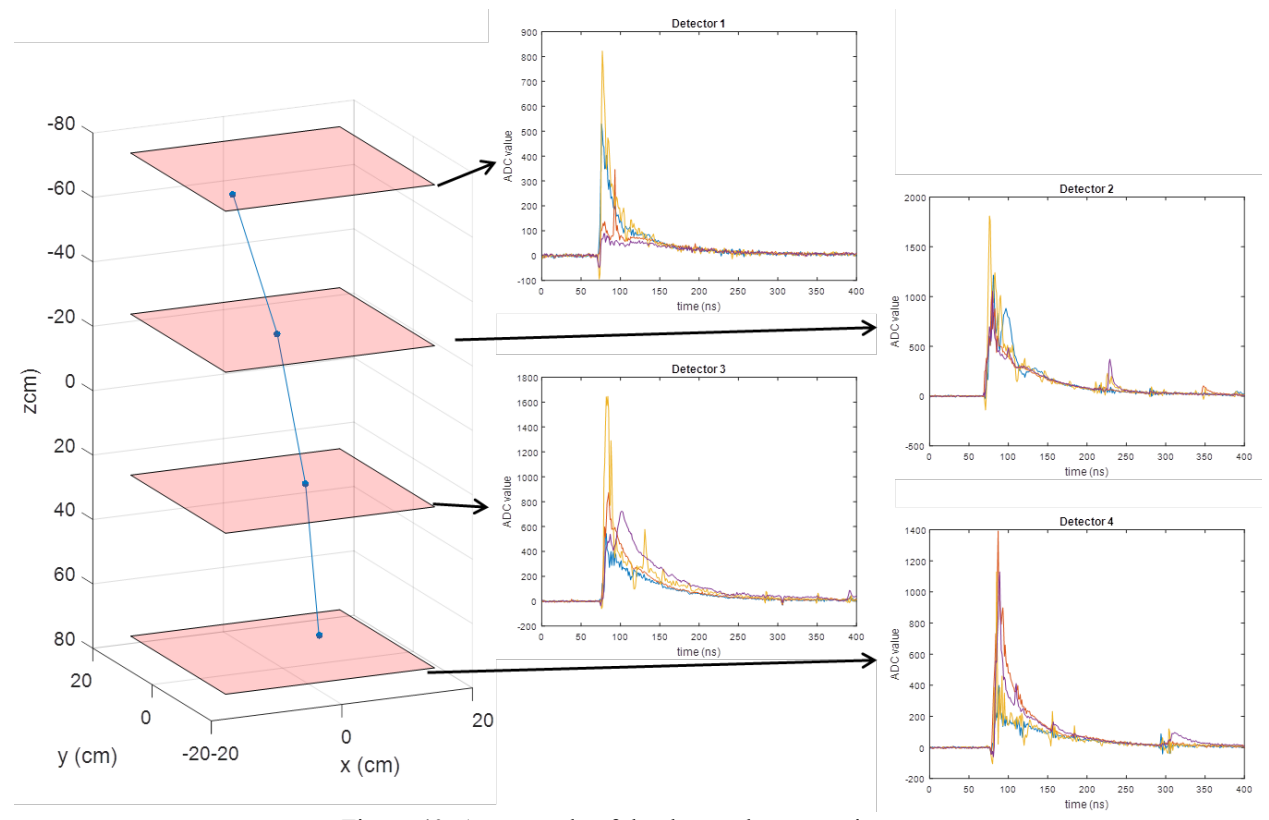


Figure 40. An example of the detected muon trajectory.

5.1.3. Debugging system design v1

Since lots of bad examples are observed in the initial test of the whole system, this section describes the effort to debug the system. Looking at the output signals, we observed some large distortions, which are possibly brought in by the signal processing PCB board. These distortions can lead to the loss of the amplitude information and therefore the loss of the position information. Thus, we optimized the circuit design by adding more space in between the components and avoiding routing traces with sharp bends. Some other minor changes are also done. Figure 42 shows the screenshot of the new design of the readout board.

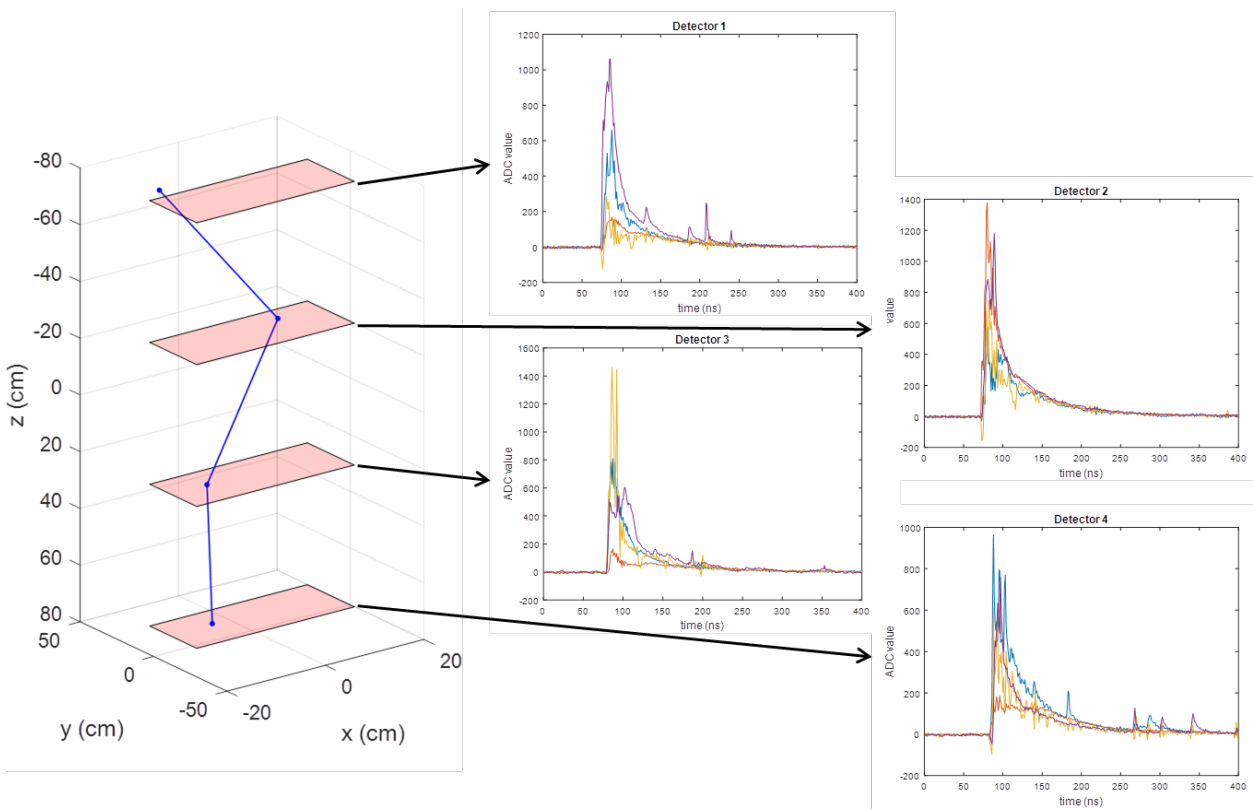


Figure 41. A bad example of the detected muon trajectory.

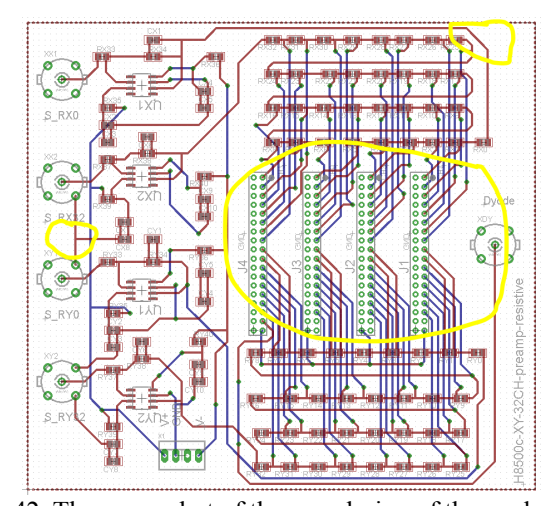


Figure 42. The screenshot of the new design of the readout PCB.

After four new boards were made, we tested each board with each detector. Since we observed signal distortions and large noise from the old version of boards, we want to avoid these problems with the new boards. Figure 43 gives a Comparison of the output signals from the old readout board and the revised board with detector 3. Clearly we see that the signals from the new board are much cleaner than those from the old board. No distorted signals are seen. All output signals follows a form of exponential decay. Unfortunately, even with the optimized circuits, large portions of bad examples are still observed in the following test. Thus, we decided to investigate another version of detector.

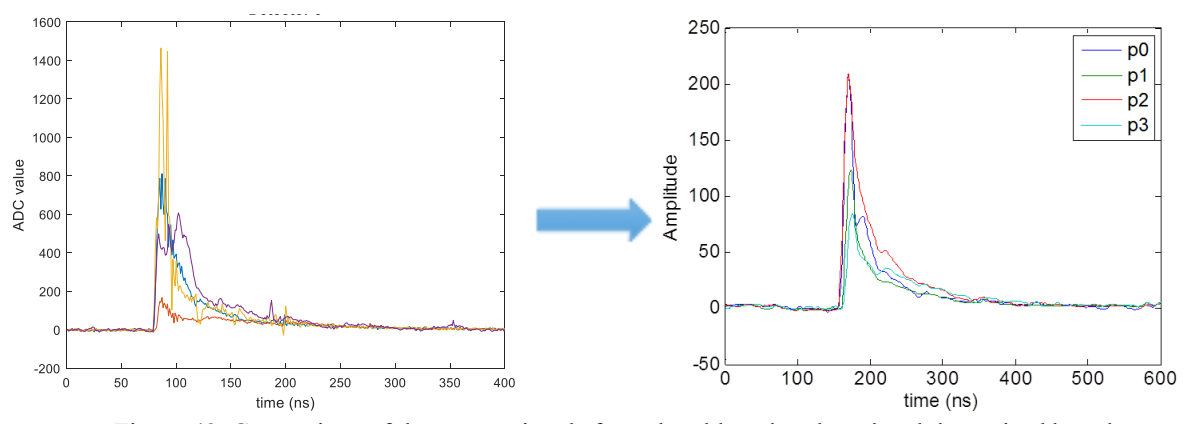


Figure 43. Comparison of the output signals from the old readout board and the revised board.

After investigating and testing the system design v1, we decided to abandon this detector design. In the previous design, a 33-resistor series was used for equivalently interpolating the 32 output channels from one dimension of one detector. The ratio of signal amplitude at two ends represents the position of interaction. However, when the interaction position comes to the edge of the scintillator, one of the signal amplitude is not significantly high to carry enough position information. In this situation the position resolution is extremely bad. Also, one interaction position relies on all 32 channels of signals. The interference between adjacent channels decreases the position resolution as well.

5.2. System design v2

In this version of design, the basic system configuration remains the same. Specifically, the system still consists of four position-sensitive muon detectors forming two muon trackers. The position-sensitive detector is composed of two orthogonal detection planes with an active area of 32 cm by 32 cm, each of which contains 32 pieces of 1 cm by 1 cm by 32 cm scintillator bars. Each scintillator bar is read out with bunches of wavelength shifting (WLS) optical fibers. One can simply get the position information by reading just one channel that has a significant signal. Figure 44 shows the schematic drawing of the second detector design. This design is called detector v2.

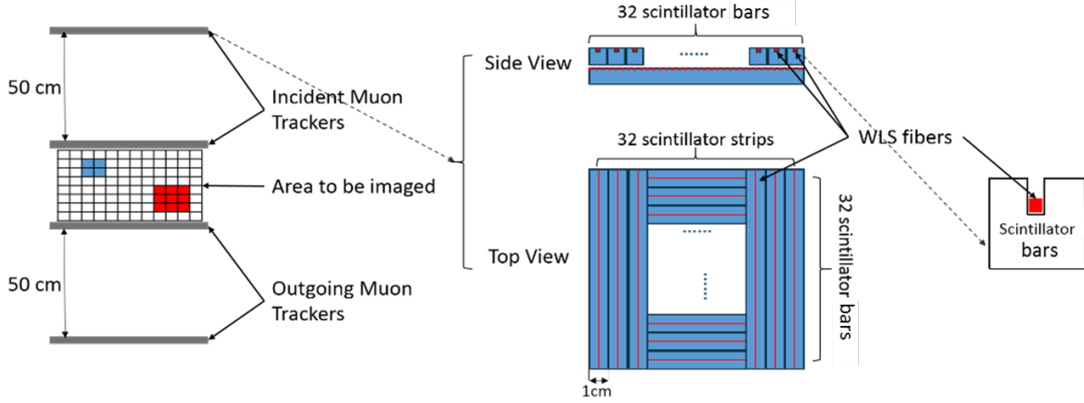


Figure 44. The schematic drawing of the second detector design using plastic scintillator bars

EJ-204 by Eljen was chosen as the scintillator material. Saint-Gobain BCF-92 WLS optical fibers were chosen for light readout. EJ-204 is another option. Their scintillation spectrum both overlaps a large portion of the absorption spectrum of the WLS fibers. The H8500C 64-pixel MAPMT by Hamamatsu has been identified as the light sensor because of its compact design and multichannel readout capability. And its response is good for reading lights from BCF-92 since it is sensitive to light whose wavelength is from 300 nm to 500 nm.

Each scintillator bar has one 1.1 mm wide and 2.0 mm deep groove on the long side in order for two 1 mm by 1mm WLS fibers can fit in it. We carefully measured the lengths of fibers needed and cut fibers to those lengths. The both ends of each fiber were carefully polished with sand paper. Then we applied EJ-550 optical grease in the groove and put the polished fibers into them. Next, the scintillators embedded with fibers were wrapped with single layer of aluminum foil. Total of 256 scintillator bars were assembled in the same method. For each muon detector, 32 scintillator bars are used for one dimension. Thus one detector needs 64 bars. Figure 45 shows a picture of a muon detector with 32 scintillator bars on each dimension. Figure 46 is the schematic drawing of the 3D printed fiber-MAPMT coupler showing the indexes of fibers and MAPMT windows.

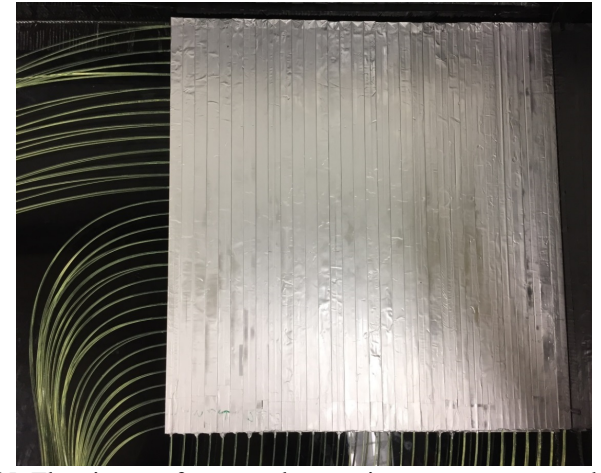


Figure 45. The picture of a muon detector in prototype system design v2.

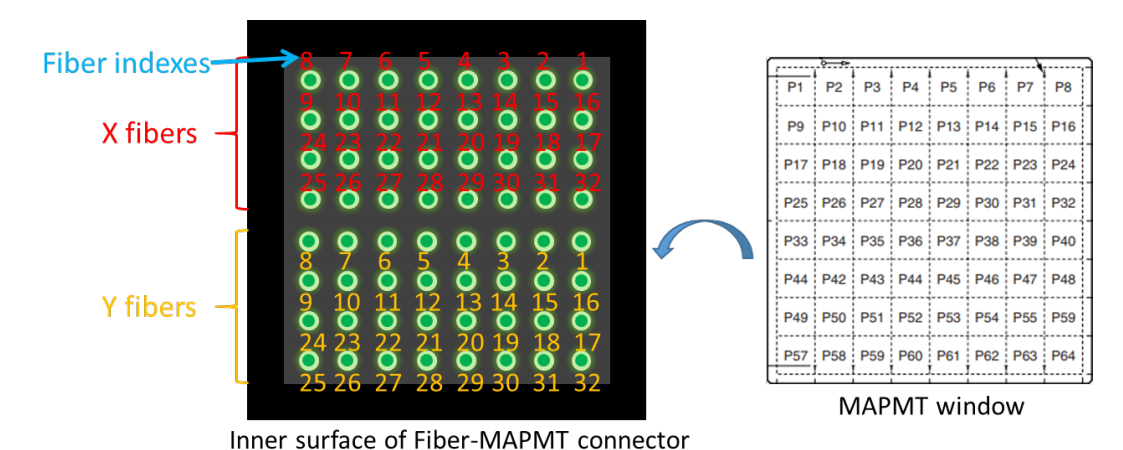


Figure 46. The schematic drawing of the fiber-MAPMT coupler showing the indexes of fibers and MAPMT windows.

Since the scintillator bars are independent from each other, we don't have to consider the interference. If all output channels are read at the same time, the interaction can be located by only considering the channel that has the most significant signals. However, this requires reading all 256 output channels at the same time. This is extremely expensive. Therefore, we went back to the traditional anger logic circuit. We use an 8 by 4 anger logic resistor network to decrease the readout channel for one dimension of one detector from 32 to 4. Figure 47 shows the idea of this 8 by 4 resistor network. Equation 4 is used to calculate the position.

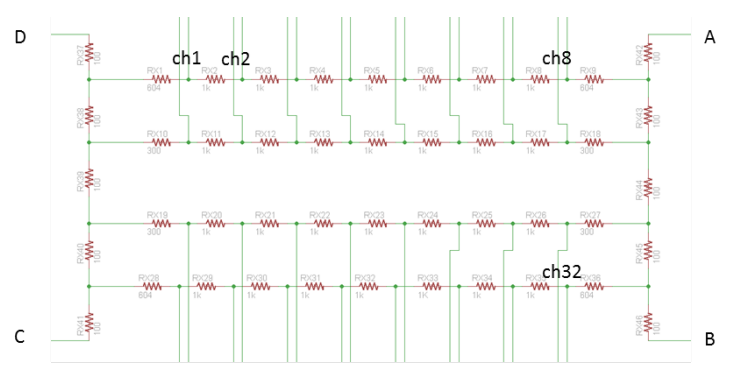


Figure 47. The circuit of the 8 by 4 resistor network

Column =
$$\frac{A+B}{A+B+C+D}$$

$$row = \frac{A+D}{A+B+C+D}$$
(4)

So in summary, one detector consists of 64 individual scintillator channels, in which 32 are for x dimension and the other 32 are for y dimension. The scintillation light from each scintillator is converted into electric signals by each corresponding PMT pixel independently. Thus one 64ch H8500 MAPMT is used for one detector. With independent 32:4 resistor networks designed for x and y channels, the total number of outputs channels needs to be acquired is reduced to 8. One dynode signal is directly outputted for one detector. Figure 48 shows the signal chain in a single detector.

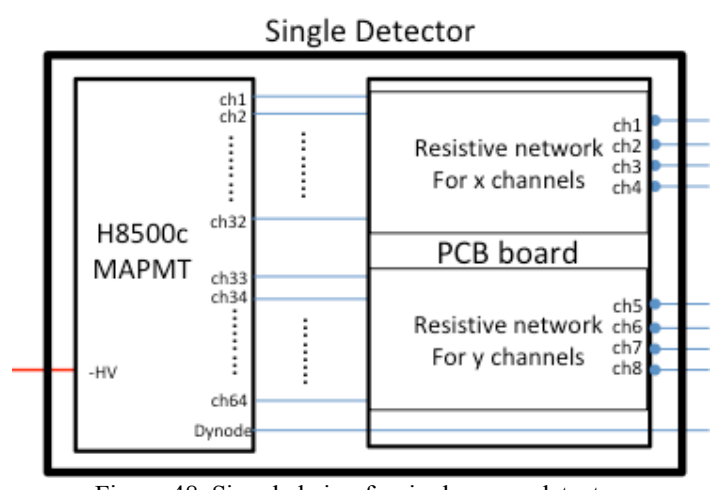


Figure 48. Signal chain of a single muon detector.

Then the 8×4 signals from resistor networks are amplified by two units of 16ch fast amplifiers from Phillips Scientific. This amplifier has fast responses and a fixed 10X gain for each channel. The amplified signals are acquired by a CAEN VX1742 32-channel Digitizer. The dynode signal from one detector ranges from several mV to 10s of mV. Thus, a preamplifier board was designed for the dynode signals. A Phillips Scientific model 710 4ch leading edge discriminator was deployed to generate trigger signals for each detector. Then the four trigger outputs from the discriminator are fed into the input of a CAEN V976B coincidence module for coincidence measurement. Then the AND output of the coincidence module is used as the trigger input of the digitizer. Figure 49 shows the signal chain for the entire system.

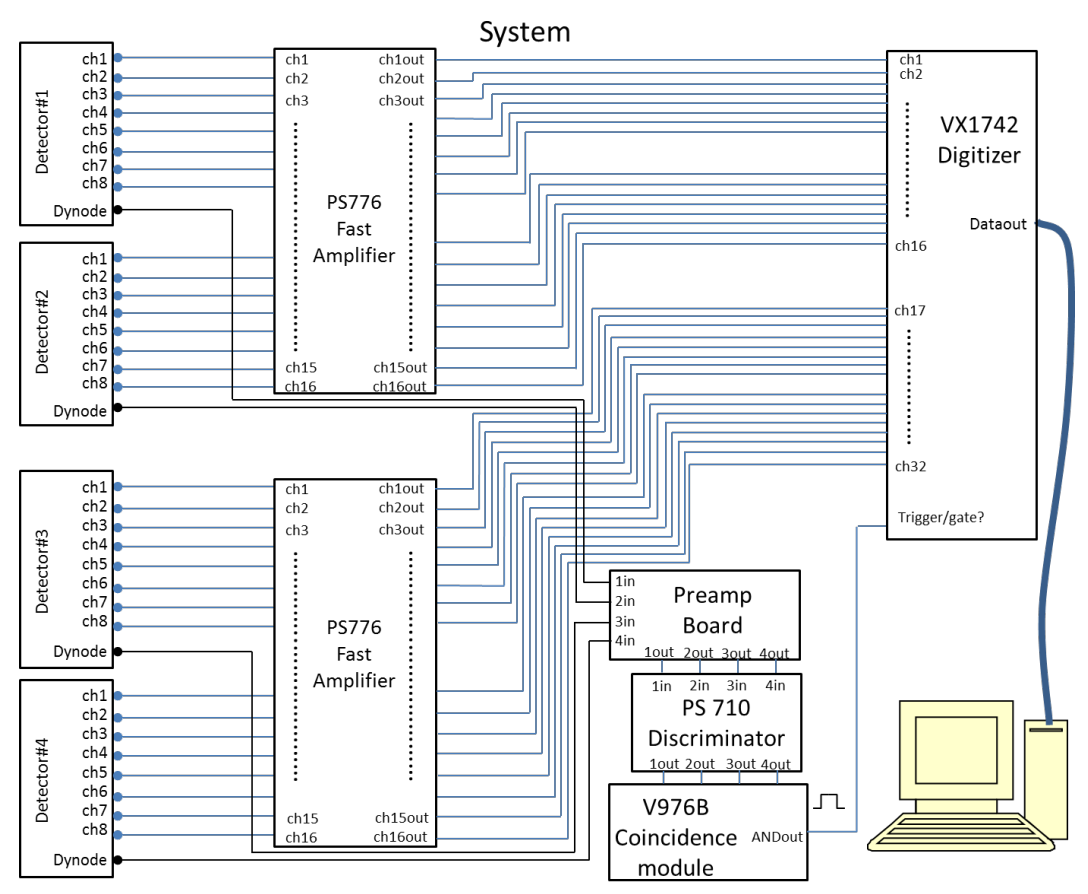


Figure 49. Signal chain of the system v2

5.2.1. Preliminary tests of system v2

5.2.1.1. Dark count measurement

First, the dark counts of each MAPMT are tested because we assume the dark counts could contribute to some false coincident events. Each PMT is not connected to any light source (scintillator or fibers) and covered carefully with black plastic bag. Then a counter was used to record the dark count rate. The resistor network boards are still used in order to find the count rate of each individual channel. The thresholds of the discriminator are all set to 20mV, which is the minimum threshold. Table 1 shows the total dark count rate. Figure 50 shows the dark count

rate map of each individual PMT, which is the dark count rate of each pixel of each PMT. As observed, the dark count rate of PMT #1 and #4 is in normal range. But the PMT #2 and #3 has a higher dark count rate especially in certain pixel. But since our system relies on coincidence, whose coincidence window is 10s of ns wide, this is not a big problem. This will be discussed in later sections. The dynode amplitude distribution given in Figure 51 also shows the higher dark count rate of PMT#2 and #3.

Table 1. The dark count rate of each MAPMT Time/s **Counts** Rate/2 Det1 60 2069 34.5 Det2 10852 60 180.9 34470 574.5 Det3 60 Det4 60 1116 18.6

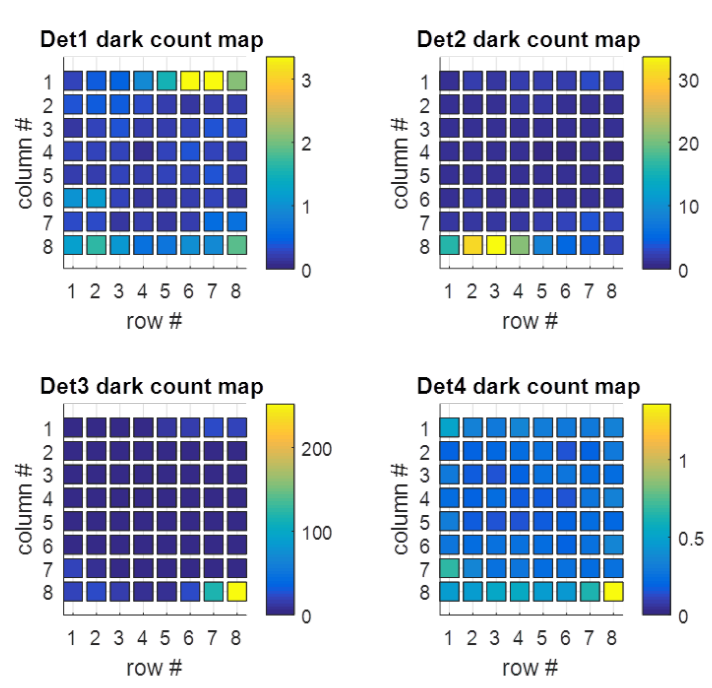


Figure 50. The dark count rate map of each individual PMT.

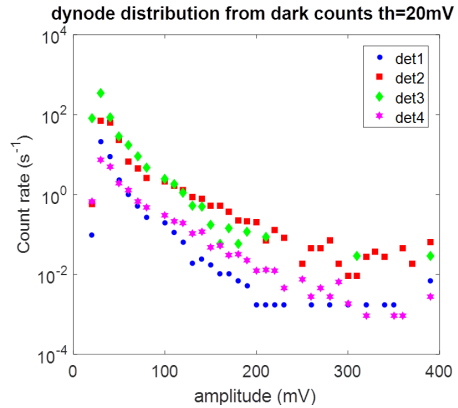


Figure 51. The dynode amplitude distributions from dark counts

5.2.1.2. Dynode signals measurement

The measurement of dynode signals for all detectors was done with natural background as well. With fully assembled detectors, the natural background count rate and dynode amplitude distribution are measured. The threshold remains 20mV for all detectors. Table 2 presents the count rate of each detector from natural background. Figure 52 shows the dynode amplitude distributions from natural background for all four detectors. The y-axis represents the count rate. So detector #2 and detector #3 have higher counts in all amplitude range. The reason is that PMT #2 and #3 have higher overall gains. Thus, in full operation, the threshold setting for detector #2 and #3 are supposed to be higher than the other two detectors to achieve equivalent background rejection performance

	Time/s	Counts	Rate/s
Det1	60	17188	286.5
Det2	60	95845	1597.4
Det3	60	51359	856.0
Det4	60	7606	126.8

Table 2. The count rate of each detector from natural background

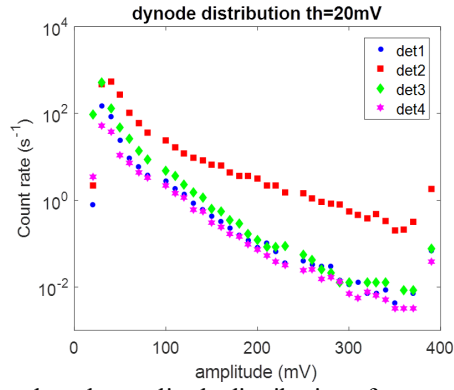


Figure 52. The dynode amplitude distributions from natural background

5.2.1.3. Coincidence rate measurement

Since muons are majorly distinguished from other radiation types through measuring coincidence, it is important to study the parameters that could potentially affect the coincident rate. The first test is to study the coincidence window width, which is the width of the trigger output of the discriminator. The discriminator threshold is set to 20mV for all four detectors. Table 3 gives the coincidence rate at given coincidence window.

Table 3 Coincidence window width vs. coincidence rate												
Coincidence window (ns)	5	10	15	20	25	30	35	40	45	50	100	150
Coincidence rate (min ⁻¹)	0	10.6	44.1	36.8	31.2	32.1	29.9	33.6	32.5	31.8	34.5	30.2

With narrow coincidence window like 15ns, one dynode signal might generate two trigger signals because the dynode signal after preamp board is not quite clean. In this case, one

effective coincidence events might generate one trigger signal and following duplicate. But when coincidence window is longer than 25ns, which is longer than the width of a dynode signal, the ripples in dynode signals do not generate false trigger signals.

The increase of the coincidence window (< 150ns) does not lead to increased coincidence rate. It is thus demonstrated that with the current background count rate, the false coincidence rate is not significant. However, shorter coincidence window always results in lower false coincidence rate with given background rate. Since muon flux is a fixed value, we can conclude that the muon coincidence rate in our system should be around 31 to 32 per minute. Thus, 25 ns coincidence window is chosen for the following tests.

As discussed in previous section, 20mV threshold is basically an arbitrarily chosen value. Thus, the thresholds for the detectors need to be optimized. Given the conclusion that the coincidence rate in our system should be around 31 to 32 per minute, when the threshold is increased but the coincidence remains the same, we can conclude that no muon events are rejected. Therefore, the coincidence rate was measured when the threshold for one detector was gradually incremented and value for other three detectors was held. The increment was stopped before the coincidence rate decreases. Then the value is taken as the threshold for this specific detector. Then the threshold setting was finalized at 30mV, 70mV, 65mV and 30mV, respectively for detector #1, #2, #3 and #4.

rabie	4. The			W C			
Table	4. The	count rate	of each	detector	from nat	tural ba	ckground

	i nresnoia/m v	Coincidence rate/s
Det1	30	102.4
Det2	70	97.7
Det3	65	159.0
Det4	30	77.8

5.2.1.4. 2D position calibration of position-sensitive detector v2

To validate the detector design v2 with the resistor network, some test was done with single scintillator bars (embedded with fibers). The test was done also with blued LEDs that were powered by a function generator. The equation 4 was used to calculate the ratio that represents the position. Table 5 shows the test results. Figure 53 shows the plot of row ratio vs column ratio. The standard deviations of the ratios are much smaller than the gap between the ratios at different position. Thus, this design improved the ability to distinguish different reaction locations.

Table 5. LED test result of the detector design v2

	Table 5. EED test result of the detector design v2.					
Channel	Column	Row	Column ratio	std	Row ratio	std
1	1	1	0.01524	0.02918	0.77979	0.01815
2	2	1	0.15033	0.01639	0.78207	0.01434
3	3	1	0.29035	0.01144	0.78375	0.01519
4	4	1	0.43511	0.00830	0.78241	0.01333
13	5	2	0.57581	0.00599	0.59478	0.00600
14	6	2	0.71748	0.00917	0.59391	0.00584
15	7	2	0.86075	0.01373	0.59341	0.00602

16	0	2	0.00522	0.01700	0.70104	0.00665
16	8	2	0.99533	0.01709	0.59104	0.00665
17	1	3	0.01063	0.02263	0.40844	0.00881
18	2	3	0.13743	0.01420	0.40616	0.00691
19	3	3	0.28705	0.00767	0.40500	0.00597
20	4	3	0.43127	0.00450	0.40397	0.00573
29	5	4	0.56959	0.00476	0.22769	0.00836
30	6	4	0.70400	0.00668	0.23105	0.00760
31	7	4	0.83257	0.00892	0.23517	0.00705
32	8	4	0.99958	0.02596	0.21350	0.01565

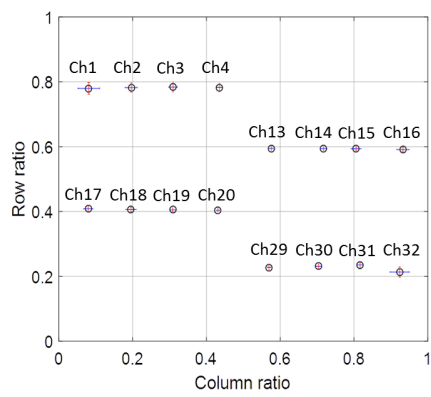


Figure 53. The plot of row ratio vs column ratio of 16 channels input.

The relationship shown in Figure 50 cannot be used to derive the positions in real test because the muon events do not produce equivalent pulses as an LED. The tolerance of the resistors and the parasitic capacitance of the board could result difference in the position-ratio relationship. Thus, we collected large numbers of sets of data for x and y dimensions of individual detectors. Then, we calculated the column ratio and the row ratio using the eight outputs signals. Figure 54 shows the scatter plot of the column ratio and the row ratio for x and y dimensions of all four detectors.

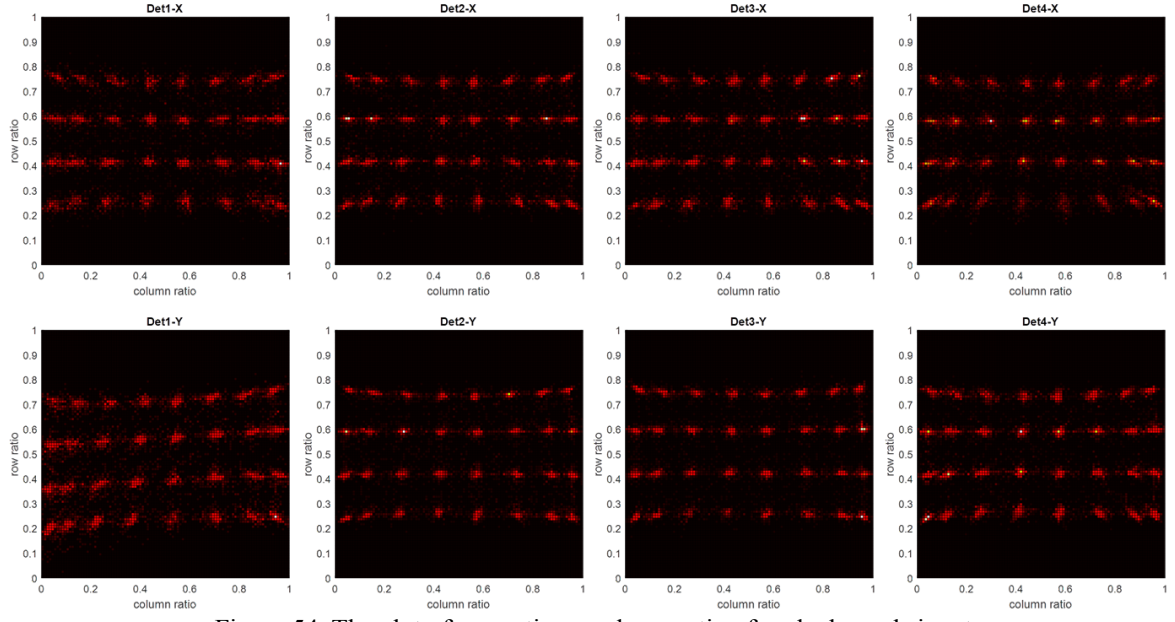


Figure 54. The plot of row ratio vs column ratio of each channels input.

Here, instead of using arbitrarily cut-off boundaries between points, an unsupervised learning method called k-nearest neighbors algorithm (k-NN) to group these points and find the center of the group. In k-NN classification, an object is classified by a majority vote of its neighbors, with the object being assigned to the class most common among its k nearest neighbors. Figure 55 shows the idea of k-NN algorithm using the x dimension of detector #1 as an example. Figure 56 shows the k-NN results for all detectors. The results demonstrated that the assumption of using the relationship shown in Figure 50 was not reliable since each map has its unique shape. Especially, for y dimension of detector y (D1y), the points in the same row don't have the same ratio value.

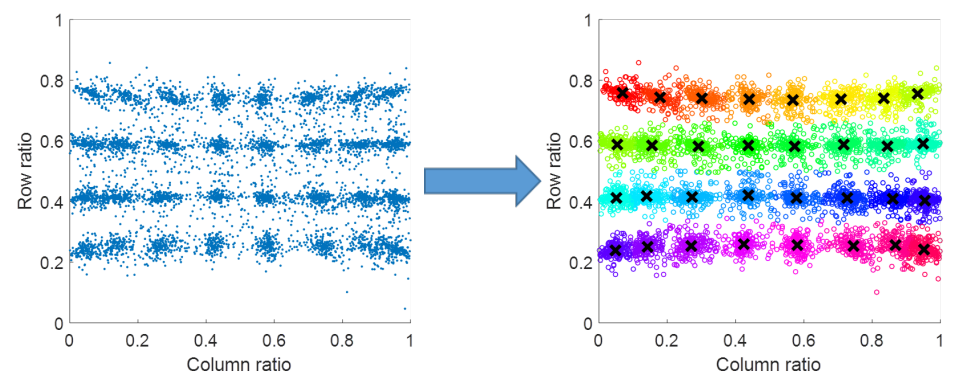


Figure 55. the idea of k-NN algorithm using the x dimension of detector #1 as an example.

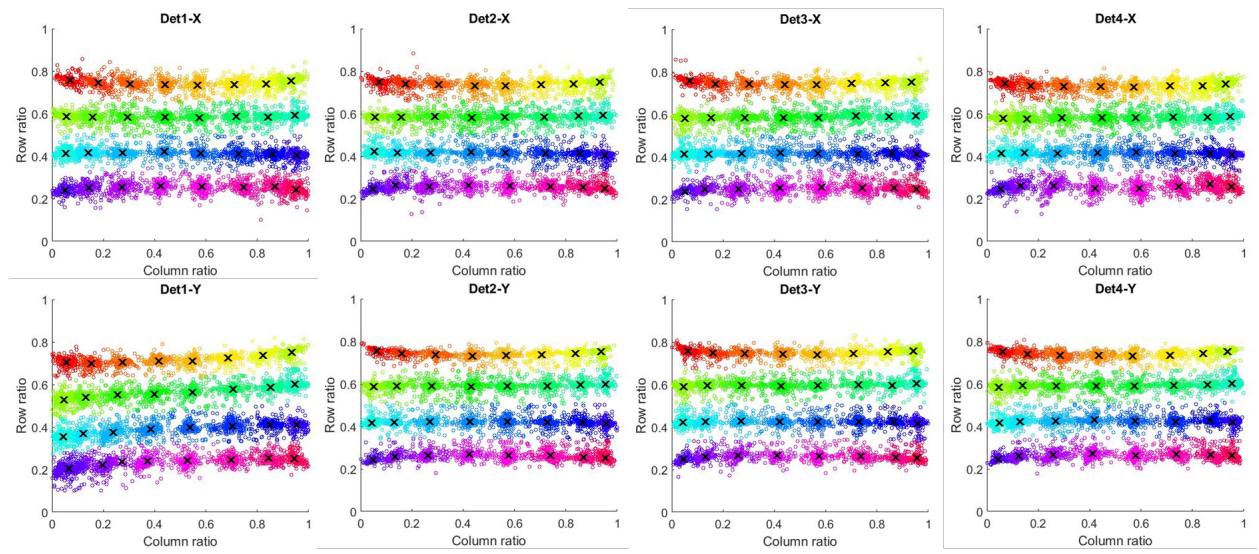


Figure 56. The result of k-NN algorithm for all four detectors.

5.2.2. Integration test of system v2

After obtaining the relationship between the ratio and position for both dimensions of all four detectors, the integration test of the entire system is performed. The test of the whole system is done with the same system configuration shown in Figure 38. The HV supply was set to 1000 V. The discriminator threshold was set to 20 mV for all four detectors for this initial test and will be optimized later. Coincidence window, which is the width of the discriminator output in our case, was set to 30 ns.

The first test was still run with no imaging objects. Ideally, the four measured muon positions on the four detectors should form a straight line when a muon event is detected by all detectors, because no significant scattering happened along the trajectories. For each registered muon events, total of 32 channels of signals are acquired. Using the digitized output signals and the position-ratio relationship shown in Figure 56, the positions can be derived, respectively for four detectors. Figure 57 shows an example of the detected muon trajectory. The four positions form a straight line as expected. The corresponding detector output signals used to extract the positon information are also shown in this figure.

The 'refracted' angle is then calculated to represent whether it is a good event. The cosine of this angle is calculated as the inner product of the directional vectors of the incoming and outgoing trajectories. The angle is calculated for x and y dimension respectively. Figure 58 shows the distributions of the 'refracted' angle in x and y dimensions. The angles are in degree. Considering the intrinsic position resolution of our detector design, the resolution of the angles can be up to 3 degrees. Thus more than 90% of the events are classified as good events.

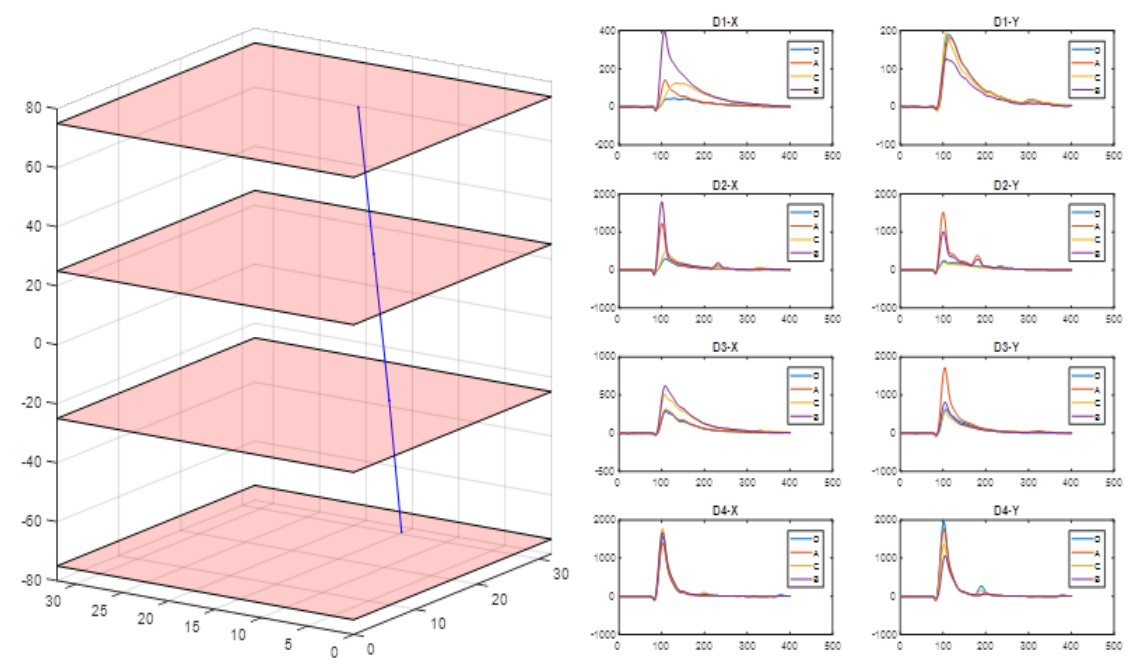


Figure 57. An example of the detected muon trajectory

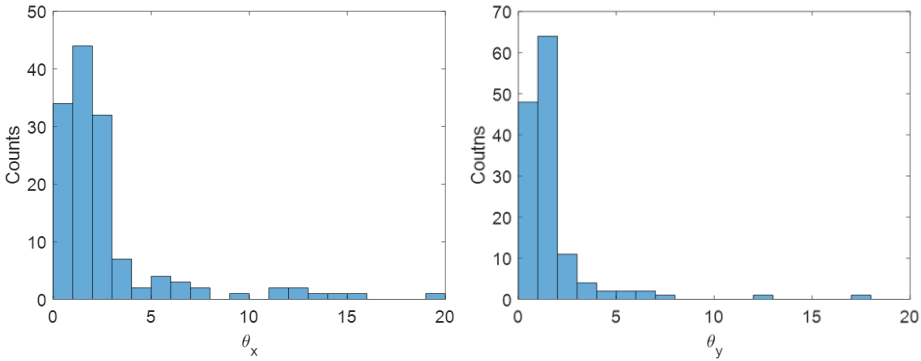


Figure 58. The distributions of the 'refracted' angles in x and y dimensions

5.2.3. Imaging simple objects with system v2

At this stage of, the system is demonstrated to function as expected. Thus, some simple objects were placed at the center layer to test the imaging capability of the prototype system v2. Since the prototype system has an active imaging area of 32 cm by 32 cm in x-y dimension and muon tomography is mainly sensitive to high-Z materials, some $20 \times 10 \times 5$ cm lead bricks were used to assess the imaging capability of the system.

Figure 59 (a) shows the photos of the image objects formed with lead bricks in the first test. The same setting was used as the integration test. The system was left running for 12 hours. The measured coincidence rate is around 32 per minute, which is close to the estimated muon coincidence rate of this system. Then, the image reconstruction was performed with POCA algorithm. Figure 59 (b) is the reconstructed image matching the based shape and size of the lead object. We can conclude our system is able to image dense objects, though with limited spatial resolution and imperfect statistical property.

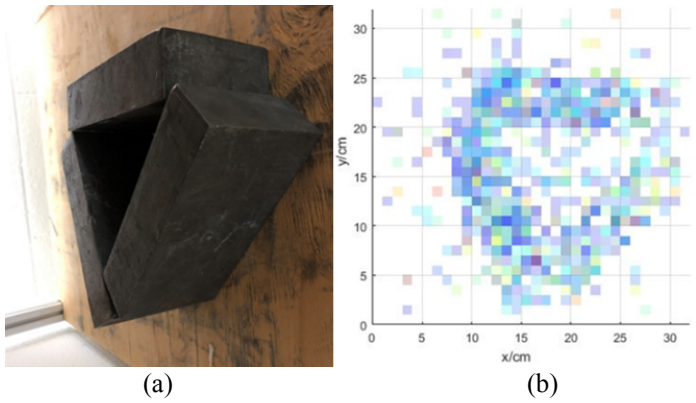


Figure 59. (a) The picture of the imaging object (b) The reconstructed image

Two more tests with different shape are also done to benchmark the image capability. This time, the imaging time is increased to 24 hours. Figure 60 shows the reconstructed images and the corresponding photos. Obviously, increasing imaging time results in better image quality.

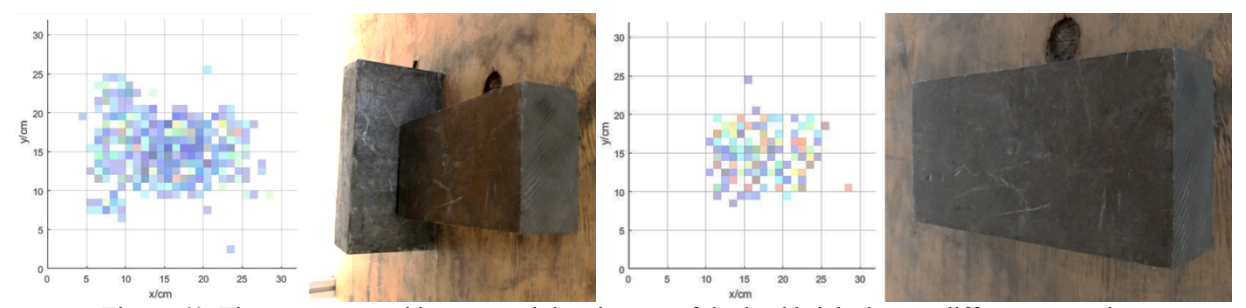


Figure 60. The reconstructed images and the pictures of the lead bricks in two different scenarios.

5.2.4. Study of the impact of additional radiation

In the previous tests, the coincidence rate stays at 31~32 per minute with the short coincidence window setting, even though the natural background rate is not low. However, the system is aimed to image a DSC that emits much higher level of radiation than background. Thus, the

impact of the radiation from a cask is necessary to be investigated. Due to the fact that we don't have the access to a DSC site, we studied the impact with some radiation sources that are accessible in out lab. Based on a report from Idaho National Lab, the average gamma dose rate from an MC-10 cask for one detector is about 1.3 mrem/hr. The neutron dose rate is about the same level. Figure 61 also shows a gamma spectrum of the cask radiation.

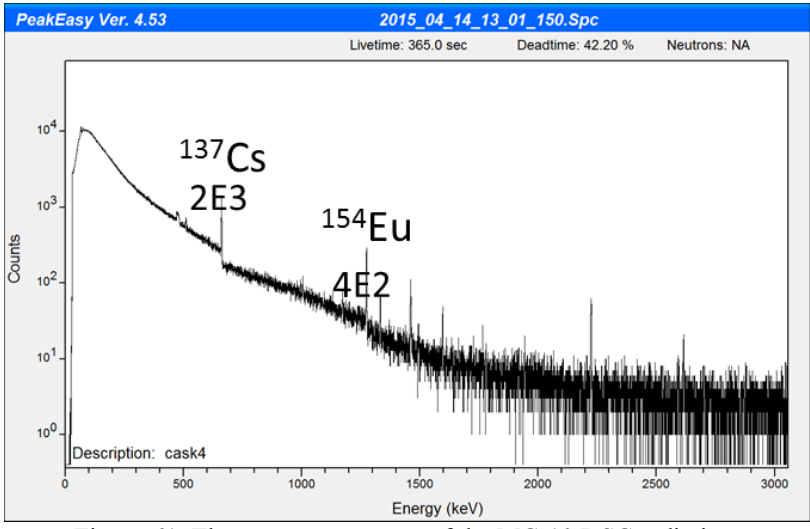


Figure 61. The gamma spectrum of the MC-10 DSC radiation.

Thus, the test was mainly done with a Cs-137 source and a Co-60 source to represent the major gamma-rays. Strong sources were positioned at a contain point so that the average dose rate at each detector is equivalent to 1.3 mrem/hr. In this part, the discriminator thresholds were set to 30mV, 70mV, 65mV and 30mV, respectively for detector #1, #2, #3 and #4. First, the count rate of each detector was measured when the radiation source were present. Table 6 listed the count rate of each detector from natural background, a Cs-137 source and a Co-60 source.

Table 6. The count rates of each detector from natural background,	, a Cs-137 source and a Co-60 source.
--	---------------------------------------

		Natural	Cs-137 ~0.7mrem	Co-60 ~1.3mrem
	Th (mV)	count/s	count/s	count/s
Det1	30	102.38	600.38	4107.08
Det2	70	97.67	349.67	2789.07
Det3	65	159.05	281.32	2034.68
Det4	30	77.75	231.97	3993.22

From the count rate results, it is observed that lots of gamma events from Cs-137 are rejected with the threshold settings. Since it is hard to estimate the real count rate of each detector from a real cask, here we exaggerate the count rate by assuming all gamma counts are from Co-60. And we assume the neutron rate is equivalent to the gamma count rate. By making a large exaggeration, the total count rate of each detector from a real cask is estimated to be 10,000 per second. The simple equation of accidental coincidence rate (ACR) is given by the following equation:

$$\mathbf{ACR} = R_1 R_2 R_3 R_4 W^3 \tag{5}$$

Using equation 5, the ACR is estimated to be 0.00156 per second. This is negligible compared to the muon rate in our system. Therefore, with largely exaggerated count rate, the ACR is negligible. However, this conclusion is not completely convincing because a point source is so different from a volume source like a cask. The result is not quantitatively valid when the actual ACR is not estimated. Without an actual cask, the quantification is barely possible.

Instead, the impact of increased ACR on image is studied. The Co-60 source was moved much closer to the detectors in this test in order to observe significantly increased coincidence rate. By doing this, the coincidence rate is increased from 31.2 per minute to 51.8 per minute. In the situation with and without Co-60 source, the same imaging objects were imaged. Figure 62 is a picture of the imaging objects formed with smaller lead models.



Figure 62. A picture of the imaging objects formed with smaller lead models

The same numbers of coincidence events were acquired for both scenarios; thus, the test without source took longer time. The images were reconstructed with POCA. Figure 63 show the reconstructed images in both scenarios. From this comparison, the increase of accidental coincidence rate does not affect the image capability and does not significantly degrade the image quality. The reason that less effective pixels are seen in the image with Co-60 is that most ACR events are rejected in the data processing stage. Majority of ACR events come from the coincidence with gamma events. The probability of a gamma event deposits energy in both layer of a detector is low. During the date processing, the inner coincidence of both layer of one detector are adopted. Therefore, most ACR are rejected. Even though the increased ACR does not significantly affect the image quality, it increases the data stream volume because the data is processed offline.

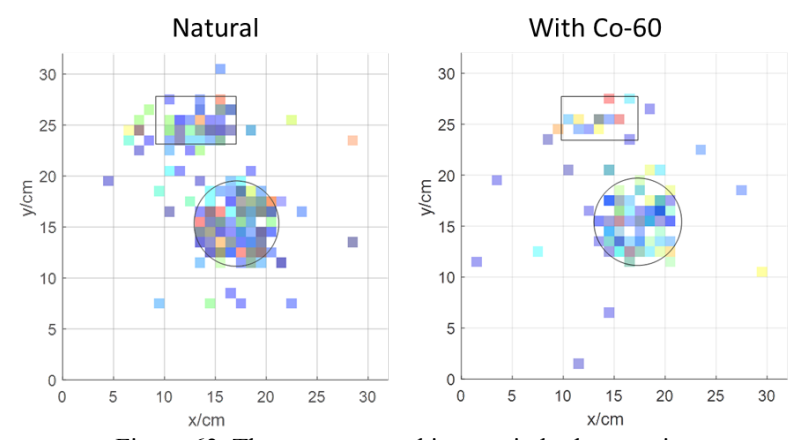


Figure 63. The reconstructed images in both scenarios.

6. Muon computed tomography algorithm studies

In conventional transmission-based medical computed tomography, x-rays are generated by a linear accelerator and then collimated to form a quasi-parallel beam before irradiating a patient or an object. The flux can vary, depending on the application, e.g., several millions photons per cm², manually controlled, and the photon trajectory is straight. The projection information is the transmission rate of x-rays, which provides integral information of the material crossed by the x-ray beam. The incident beam often has significant probability of experiencing Compton scattering in an object, which can scatter x-rays at large angles. Scattered x-rays either are not registered by detectors or are registered by bins other than the bins hit by the uncollided x-rays, causing noise in the signal.

Contrary to x-rays, cosmic ray muons are naturally generated from the decay of pions, which are the products of interactions between primary cosmic rays and upper atmospheric atoms. The result is an uncollimated flux of particles at a low flux rate of approximately 1 muon/cm²/minute at sea level. In addition, the muon flux depends strongly on zenith angle and altitude. As charged particles, when muons pass through matter, they lose energy via ionization and are deflected from their incident direction via MCS from nuclei **Error! Reference source not found.** Since the energy spectrum of muons is continuous, and the average range is sufficient to allow the majority of muons to pass through most objects, both differential attenuation and scattering could be used to provide signals and generate tomographic images of the stored contents. It has been shown that the variance of the scattering angle is more sensitive to atomic information than attenuation **Error! Reference source not found.**

In both x-ray and muon CT, filtered back-projection (FBP) and algebraic reconstruction techniques (ART) can be used to reconstruct objects under investigation. A comparison of x-ray CT and muon CT is shown in Table 7. The non-straight muon path and the use of scattering angles instead of transmission necessitates the development of a new imaging framework that includes ray tracing and projection techniques and can be coupled with FBP or ART. A new theoretical framework to enable muon CT is proposed in the following section.

Table 7.	V	OT		CT
Table /.	A-rav	C I VS	muon	C I

	x-ray tomography	μ tomography
Source	linear accelerator	Cosmic ray muon
Flux rate	Very high	Very low (1muon/cm²/minute)
Use collimator	Yes	No
Path type	Straight	Non-straight
Integral information	$\frac{I}{I_0}$	$\sigma(\theta)$ or $\frac{I}{I_0}$
Tomography modality	Transmission	Scattering or Transmission (scattering is more sensitive atomic number)
Reconstruction methods	FBP ART (SIRT SART)	FBP ART (SIRT SART)

6.1. Proposed framework for muon CT

6.1.1. Projection information

In x-ray CT, let I_0 and I be the incident and outgoing beam intensity, respectively. The ratio $ln(I/I_0)$ is used to reconstruct an object under investigation using FBP or ART as shown in Figure 64 Error! Reference source not found.

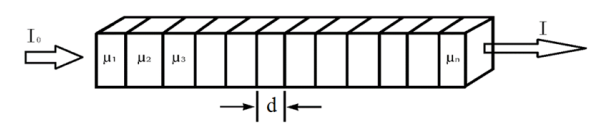


Figure 64. Illustration of neutral beam crossing a discretized object.

In Error! Reference source not found., the attenuated intensity I can be described by:

$$I = I_0 e^{-d\sum_{i=1}^n \mu_i} \tag{6}$$

where d is a selected discretized length in cm and μ_i is the attenuation coefficient of the i^{th} pixel in cm⁻¹. After rearrangement,

$$\ln\left(\frac{I_0}{I}\right) = d\sum_{i=1}^n \mu_i \tag{7}$$

The signal obtained from one projection or view is not enough to reconstruct an image. One typically rotates the radiation source and the detectors, while the object remains stationary, to obtain additional information from different angles.

In μ CT, the incident source is naturally occurring cosmic ray muons. Most muons transmit through objects, especially muons with high momentum (compared with the mean that falls in the range 3-4 GeV). When muons traverse an object, many different scattering angles are registered, following a Gaussian distribution with zero mean value and variance given by Eq. (10). The concept of a muon traversing an object is shown in Figure 65 Error! Reference source not found.

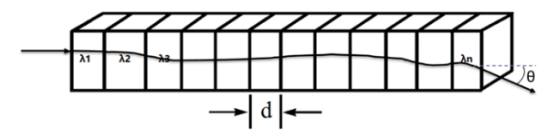


Figure 65. Illustration of a muon traversing a discretized object. The magnitude of the scattering angle is exaggerated in the figure for illustration purposes.

The variance of scattering angle of a muon beam caused by the ith voxel is given by:

$$\sigma_{\theta_i}^2 = d\lambda_i \tag{8}$$

where λ_i is the scattering density of the ith pixel. The scattering density is defined as **Error!** Reference source not found.:

$$\lambda(L_{rad}) \equiv \left(\frac{15}{p_0}\right)^2 \frac{1}{L_{rad}} \tag{9}$$

where p_0 is the nominal momentum. In this work, p_0 is chosen to be 3 GeV/c. Since MCS in individual pixels can be treated as independent, the variance of scattering angle of a muon beam after traversing the entire object may be written as:

$$\sigma_{\theta}^{2} = d\sum_{i=1}^{n} \lambda_{i} \tag{10}$$

Note that Eqs. Error! Reference source not found. and Error! Reference source not found. have the same form; i.e., the right side of these two equations is a linear integration of a parameter over the particle's path. Thus, the scattering density λ may be treated similar to the attenuation coefficient μ used in the computed tomography image reconstruction process.

In order to obtain parallel or quasi parallel muon beams, the detectors were rotated around objects under interrogation for 180 degree. Only muons crossed four detectors were used below otherwise it was discarded. Let the position of ith muon be (x_{1i}, y_{1i}, z_{1i}) , (x_{2i}, y_{2i}, z_{2i}) , (x_{3i}, y_{3i}, z_{3i}) , and (x_{4i}, y_{4i}, z_{4i}) on the four detectors separately, from left to right. The azimuth component of the incident angle φ_i is

$$\varphi_{i} = \arctan\left(\frac{y_{2i} - y_{1i}}{x_{2i} - x_{1i}}\right) \tag{11}$$

All registered angles were then sorted into quasi-parallel ray data sets during data processing. The scattering angles θ_i were calculated using:

$$\begin{aligned} \theta_{iy} &= \text{atan} \left(\frac{y_{4i} - y_{3i}}{z_{4i} - z_{3i}} \right) - \text{atan} \left(\frac{y_{2i} - y_{1i}}{z_{2i} - z_{1i}} \right) \\ \theta_{iy} &= \text{atan} \left(\frac{y_{4i} - y_{3i}}{z_{4i} - z_{3i}} \right) - \text{atan} \left(\frac{y_{2i} - y_{1i}}{z_{2i} - z_{1i}} \right) \\ \theta_{i} &= \sqrt{\frac{\theta_{ix}^{2} + \theta_{iy}^{2}}{2}} \end{aligned} \tag{12}$$

Using each muon's momentum to correct for the influence of polyenergetic muons, in this work the nominal momentum p_0 is chosen to be 3 GeV/c. p_i is the initial momentum and no energy loses during the process of crossing objects. If no momentum information is assumed in the following reconstruction process, this step is simply skipped.

$$\theta_i' = \frac{p_i}{p_0} \theta_i \tag{13}$$

Due to the uniformity along Z axis of our imaging object, after incorporating the path length into correction for the influence of different path length, the normalized scattering angle of a muon becomes

$$\theta_i^{"} = \frac{L_{ih}}{L_i} * \sqrt{\frac{D}{L_i}} * \theta_i^{"} \tag{13}$$

where D is the vertical distance between detectors 2 and 3, L_i is the distance between (x_{2i}, y_{2i}, z_{2i}) and (x_{3i}, y_{3i}, z_{3i}) , and L_{ih} is the horizontal projection of L_i . Finally, the registered incident muon spectrum was divided into one-degree-wide azimuthal bins according to their incident horizontal direction angles φ , re-sorting the incident muons into 180 quasi-parallel groups and projected to a horizontal plane.

6.2. Muon tracing methods

Three different muon tracing methods, namely (1) straight path along incident horizontal trajectory, (2) straight path along incident horizontal direction crossing PoCA point, (3) POCA trajectory. Two different projection methods on how to use the scattering angle: (a) each scattering angle is used only once and stored directly into corresponding detector bins, (b) each scattering angle were back projected into image space first to calculate variance of scattering angle in each pixel then forward project the summation of variance to corresponding detector bins. Six possible methods 1a, 1b, 2a, 2b, 3a and 3bwere used to generate projection information and system matrix to investigate how muon ray trace model and angle projection method affect muon CT capabilities, like reconstruction image quality and detection capability. Muons from any quasi-parallel beam subset are considered below. Only the detectors are retorted for each subset.

6.2.1. Method 1: Use of a straight path along the incident muon trajectory

This method assumes that muon experiences no scattering event or the scattering is negligible resulting a straight muon path crossing the object along its incident trajectory. Two different means are used to project scattering angle along this trajectory: method 1a is to directly store the scattering angles for each muons from the same quasi-parallel beam subset into the corresponding detector bins hit by its path, then calculate the variance of scattering angle in each bin as projection information P; Method 1b is to back project the each scattering angle into the Figure

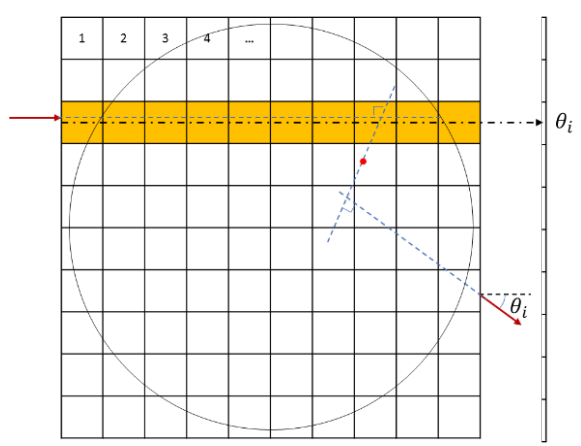


Figure 66. Top-down view illustration of method 1. Method 1a projects the scattering angle within a defined volume (shown as a large square) along a straight line to a segmented detector (shown at far right). In method 1b, θ_i is back projected into the pixels crossed by this straight path indicated the yellow strip. See the text for details.

pixels crossed by this straight path for all muons in the same quasi-parallel beam subset first and then calculate the variance of scattering angle in each pixel, finally take the summation of the variances along this path and store it into corresponding detector bin as projection information P. Both filtered back projection (FBP) and simultaneous algebraic reconstruction technique (SART) were used to reconstruct image with the projection information P. For FBP, simply apply a high pass filter to projection information P stored in the detector bins before back projecting them into the space domain. For SART, the average path length in each pixel is used to build system matrix W as shown in Figure 66.

6.2.2. Method 2: Use of a straight path along the muon incident direction that crosses the PoCA point

This method assumes that a muon experiences a single coulomb scattering event within a defined volume. The scattering angle is caused by this event happened at the closest distance between the incident and exiting trajectories. This point is also known as the PoCA point. Instead of completely ignoring the exiting position, method 2 made a compromise between the incident and exiting positions by assuming muon crossed object along incident direction crossing PoCA point as shown in Figure . The rest steps are similar to that described in method 1.

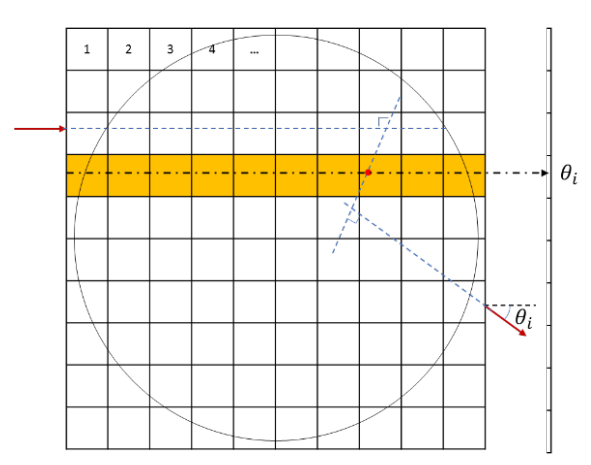


Figure 67. Top-down view illustration of method 2. Method 2a projects the scattering angle within a defined volume (shown as the large square) along a straight line to a segmented detector (shown at right). In method 2b, θ_i is back projected into the pixels crossed by this straight path indicated by the yellow strip. See the text for details.

6.2.3. Method 3: Use of PoCA trajectory

Due to the nature of charged particle, muon would experience multiple coulomb scattering during the process of traversing objects causing deviation from a straight path. Thus a curve path may better approach muons trajectory crossing objects than a simple straight line. This method assumes that a muon travels along the so-called PoCA trajectory within our defined volume. The PoCA trajectory consists of two segments: (1) the segment connecting the point of muon incidence to the PoCA point and (2) the segment connecting the PoCA point and the point at which the muon exits said volume as descried in Figure . The rest steps are similar to that described in method 1.

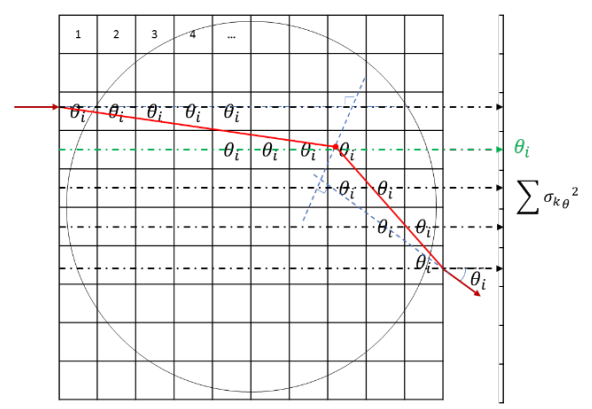


Figure 68. Top-down view illustration of method 3. According to method 3b, the scattering angle is projected back into the pixels crossed by the PoCA trajectory for all muons in a quasi-parallel beam subset, the variance in each pixel is calculated, and the sum of the variances along each dot dash line is stored in corresponding detector bins. In method 3a projects the scattering angle along a straight line in green to a segmented detector (shown at far right) and system matrix is calculated with the PoCA path indicated by the red segments.

6.2.4. Method 4: Most probable trajectory

Method 1 assumes no scattering event and methods 2-3 heavily rely on PoCA to determine the muon path. However, the PoCA assumption has certain limitations. A major limitation (see Figure) is the possible allocation of the PoCA point outside the region of interest. Such points need to be rejected otherwise cause noise, reducing the useful muon flux for image reconstruction. It was found that rejected PoCA events made up ~30% of the total muons Error! Reference source not found. This disadvantage can be alleviated by estimating the most probable trajectory (MPT) of a muon when it traverses an object. The MPT algorithm used in this work, described in detail in Error! Reference source not found. [Error! Reference source not found., employs a bivariate Gaussian approximation of MCS with the generalized scattering and displacement moments to estimate the path of a muon in uniform or non-uniform geometries. A representative example of an individual muon path obtained from Geant4 (solid line) and the corresponding straight-line path (SLP), PoCA and MPT approximations is shown in Figure . In this case, the SLP does not accurately capture the muon trajectory, whereas the PoCA falls outside of region of interest. Instead, the MPT algorithm is in good agreement with the simulated muon path

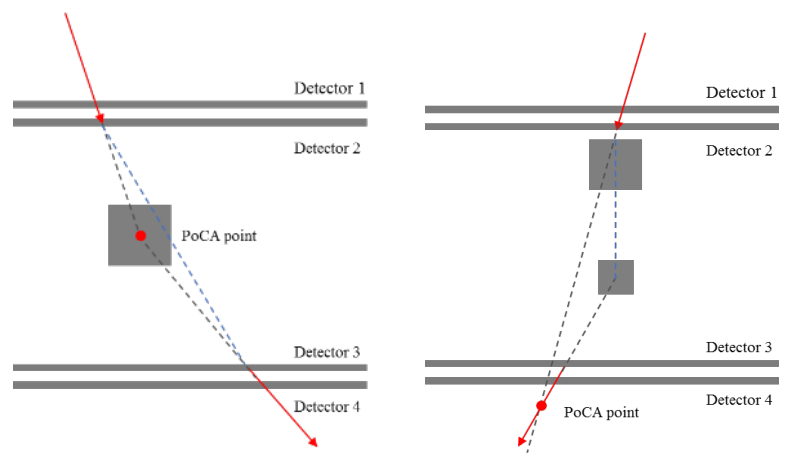


Figure 69. Illustration of possible PoCA assignments (red dot) for different high Z volumes being imaged.

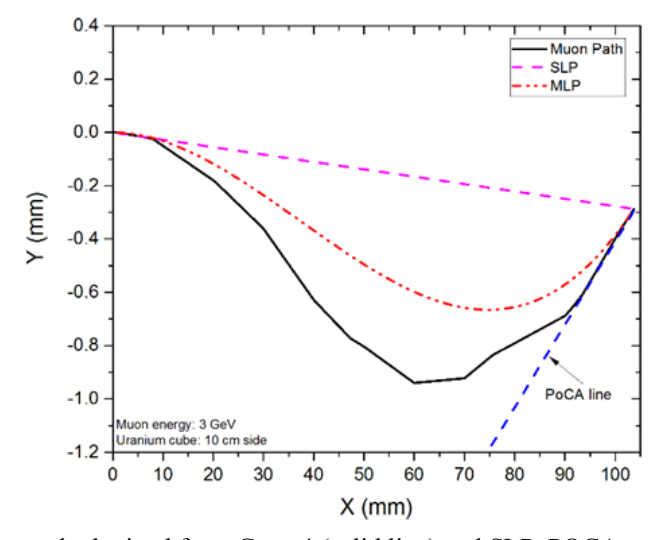


Figure 70. Individual muon path obtained from Geant4 (solid line) and SLP, POCA, and MPT approximations[38]

To obtain projection information using the MPT approach, scattering angles for all muon in a quasi-parallel beam subset are back projected into pixels crossed by the MPT. Next, the variance of scattering angles is calculated in each pixel, and variance is again summed along incident direction and stored in corresponding detector bins. The concept is illustrated in Figure .

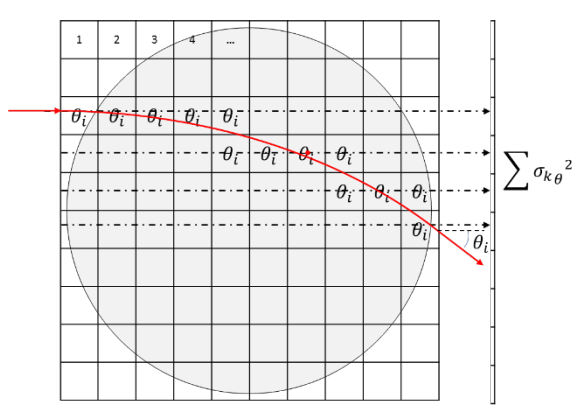


Figure 71. Illustration of method 4b for projecting the scattering angle along the MPT trajectory.

6.3. Image reconstruction

In this work, the reconstruction was implemented using both FBP and a simultaneous iterative reconstruction technique. The detail about FPB method is outside the scope of this research. A total of N=90 angular views were used. The object to be reconstructed was digitized into 100×100 pixels, and the scattering density was expressed as a $100^2\times1$ vector X. Each projection may be analytically expressed as an integration of scattering density along the path:

$$P_{\theta}(R,\theta) = \iint f(x,y)dxdy \tag{14}$$

where f(x, y) is the scattering density at position (x, y). Similarly, if we discretize the reconstruction volume, this could be expressed numerically as:

$$WX = P \tag{15}$$

where W is the system matrix containing the average path length and X is the scattering density map of the object to be reconstructed, and P is the projection information. SART can be used to solve Eq. (15), which is **Error! Reference source not found.**:

$$X_{j}^{(K+1)} = X_{j}^{(K)} + \frac{\lambda \sum_{i} \left[w_{ij} \frac{p_{i} - \overline{w}_{i}^{T} X^{(K)}}{\sum_{j=1}^{N} w_{ij}}\right]}{\sum_{i} w_{ij}}$$
(16)

The iterative reconstruction process is stopped when the maximum iteration number is reached or when the difference in successive iterations is below a threshold. In this paper, relaxation $\lambda = 0.45$ and 100 iterations were chosen.

6.4. Validation & code benchmarking

Prior to muon dry cask simulations, the use of GEANT4 to simulate cosmic ray muons through high-Z objects was validated. Two sets of test data were used for validation and code benchmarking: a set of actual muon dry nuclear fuel cask results from a recent experiment performed by Los Alamos National Laboratory (LANL); and a set of theoretical data for six different materials.

6.4.1. Validation against experimental results

We first started with a GEANT4 model validation of a physical experiment done by LANL **Error! Reference source not found.** LANL used their muon detector system to make measurements beside a partially loaded MC-10 dry storage cask located at the Idaho National Laboratory cask farm. This cask was filled with 18 out of 24 PWR fuel assemblies (see Figure 72). Muon tracking detectors were placed on opposite sides with a relative elevated difference of 1.2 m. A total of 9 measurement configurations were realized by placing the detectors at different horizontal positions. Each configuration collected 4×10^4 to 9×10^4 muons.

For validation purposes, the exact same MC-10 dry storage cask, loading pattern, and detector configuration were simulated in GEANT4 in an effort to reproduce the experiment. Muon detectors were shifted 6 times in total, as described in [38]. Radiation emitted from the cask was not simulated, and the detectors were modelled to have 100% efficiency. A simple PoCA method was used to generate an expected muon scattering angle map in the dry storage cask. The expected mean scattering angle was calculated, and it was compared to reported measurement data. Figure 73 shows a comparison of average scattering angle in a slice horizontally crossing the center of the cask between the experimental result and our simulated result. The results show that our simulation is relatively close to the data from the experiment, except the region from about -20 cm to 40 cm, which might be attributed to the detector motion in the field experiment and the damage of partial drift tubes in the detectors. An obvious peak for column 2 relative to column 1 is expected due to the existence of a fuel assembly in the column.

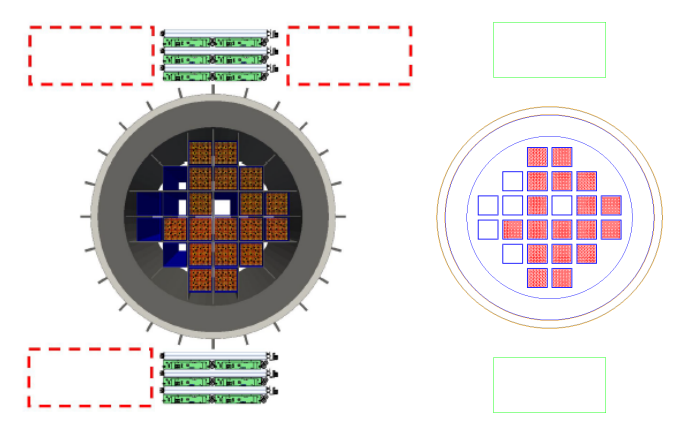


Figure 72. MC-10 cask configuration used in LANL experiment (left) and GEANT4 simulated cask (right).

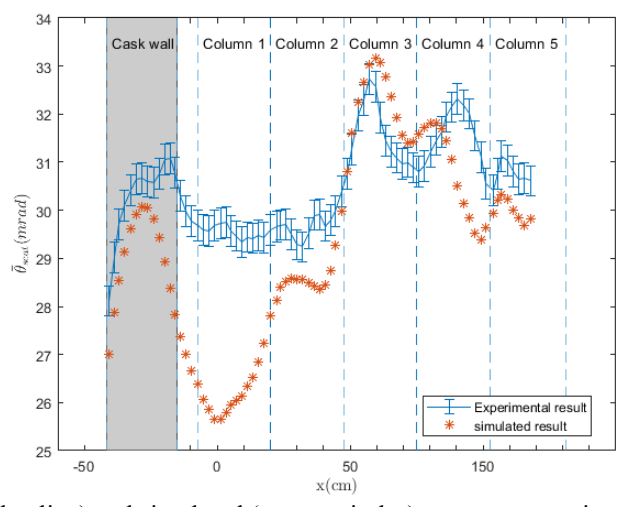


Figure 73. Experimental (blue line) and simulated (orange circles) average scattering angles for muons crossing a MC-10 dry storage cask [38].

6.4.2. Code benchmarking using analytical data

Furthermore, six cubes made of solid Al, Fe, Cu, Pb, W, or U were simulated using GEANT4 to investigate expected muon CT material discrimination capability for a simple geometry. The cubes were placed between two pairs of position sensitive detectors. Parallel monoenergetic

muons were generated. The muon source and detectors were rotated simultaneously 90 times at an azimuthal angle increment of 2° to generate 90 views. The pixel sizes of either 1×1 cm or 2×2cm were used in the reconstruction process. The configuration is shown in Figure 74. The scattering angles were registered for each muon, and method 1a with FBP was used for reconstruction. The reconstructed image is shown in Figure 74. The simulated and reconstructed images show very good agreement.

Next, the scattering density of each cube was calculated analytically with eqn (4) and was compared with the reconstructed values for two pixel sizes, 1×1 cm² and 2×2 cm². The actual and reconstructed scattering densities are shown in Table 8. Although slightly different values are observed between the actual and reconstructed scattering density, the values are within 3σ . The larger deviations can be attributed to shadowing from the surrounding materials. These results suggest that the proposed muon CT framework may be able to accurately reconstruct both geometrical and material information in most cases, at least in a simple geometry like this one.

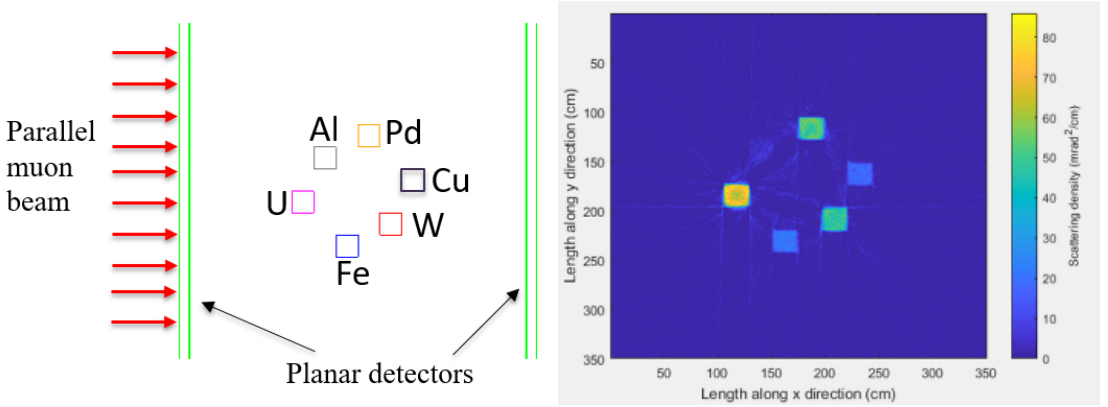


Figure 74 Top-down view of configuration of six cubes, detectors and muon beam (on the top) and corresponding reconstructed image (at bottom).

Table 0	A atrial a	nd estimated	acottorina	donaitre	for different	motoriola
Table 8	Асшага	na estimatea	scarreng	aensiiv	tor aitterent	materials

Material	Scattering density					
		(mrad²/cm)				
	Actual	Reconstructed	Reconstructed			
		(pixel=1 cm)	(pixel=2 cm)			
Al	2.81	4.5±2.9	4.4±2.5			
Fe	14.22	17.8±3	17.8±1.5			
Cu	17.41	21.0±4	21.0±1.4			
W	71.35	54.5±4	52.3±2.6			
Pb	44.55	47.6±5	47.5±2			
U	78.96	72.2±7	71.3±4			

6.5. Results and discussion

6.5.1. Test model configuration

The Monte Carlo code GEANT4 was used to simulate a VSC-24 dry cask Error! Reference source not found. This cask contains the fuel assemblies in a thin steel canister that is shielded by a thick concrete overpack. This configuration is notably different than the MC-10 cask measured by LANL; a VSC-24-type cask is widely used for storing spent nuclear fuel and was selected to better represent the dry storage cask population. The simulated dry cask geometry is illustrated in Figure 75. The dry cask was fully loaded with one fuel assembly missing from row 3. Two pairs of planar detectors 350cm×150cm, vertically offset by 100 cm and positioned along the sides of the dry cask, were simulated. For either pair, the separation between each detector was 10 cm. The zenith angle was ~50°, yielding a muon flux of ~20,000 muons/min.

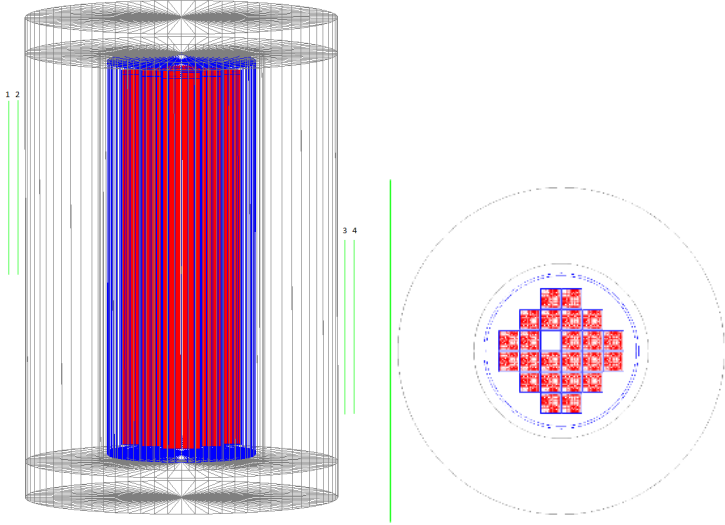


Figure 75. Side (left) and top-down (right) illustrations of the cask and detectors built in Geant4. An assembly has been removed from column 3.

The detectors were planes with perfect spatial and energy resolution. The muon event generator described in **Error! Reference source not found.** was used to simulate the muon flux at sea level. In our implementation, the cask containing the spent fuel assemblies was fixed, and the detectors rotated around it. The detectors were rotated at 2° increments to collect data from multiple views.

6.5.2. Results

We started with a dry storage cask with one fuel assembly missing as shown in Figure , 7.1×10^6 muons were to reconstruct the image, which is equivalent to 18.7 hours exposure with the configuration. 6 methods, namely 1a, 1b, 2a, 2b, 3a, 3b were used to reconstruct the dry storage cask with one spent nuclear fuel missing in the middle. The results with using muon momentum information are shown in Figure 76, 77 and results without using muon momentum information are shown in Figure 3, 79. Compared to FBP, algebraic techniques are more useful when ray path is subject to bending on account of refraction and scattering, or when the energy propagation undergoes attenuation or when it is under sampling. Thus most of the following

results are based on SART, but FBP was used in method 1a and 1b for the purpose of comparison.

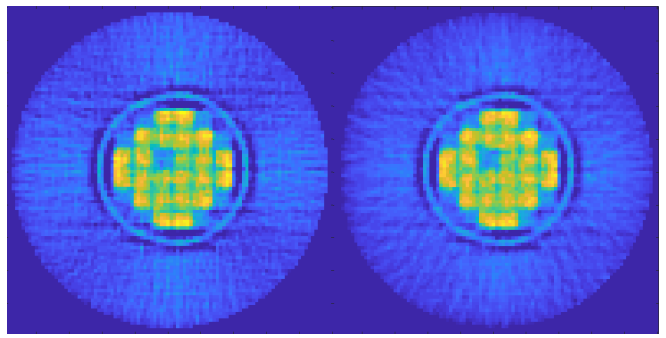


Figure 76. FBP reconstruction of a dry cask referring Figure with momentum measurement. Results are shown using method 1a on the left and method 1b on the right.

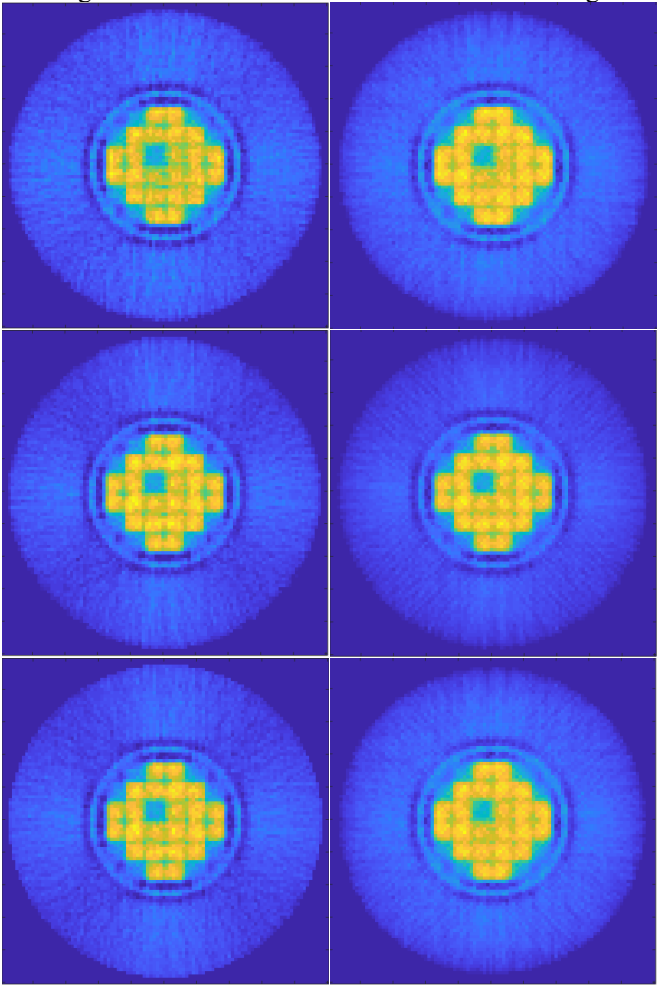


Figure 1. SART reconstruction of a dry cask referring Figure with momentum measurement. Results are shown using method 1a (top-left), method 2a (middle-left), method 3a (bottom-left) and method 1b (top-right), method 2b (middle-right), method 3b (bottom-right).

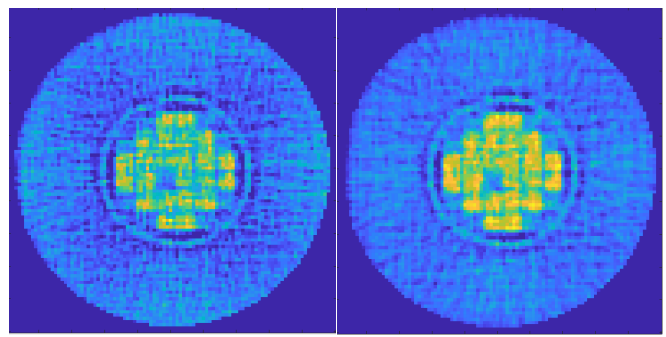


Figure 2. FBP reconstruction of a dry cask referring Figure without momentum measurement. Results are shown using method 1a on the left and method 1b on the right

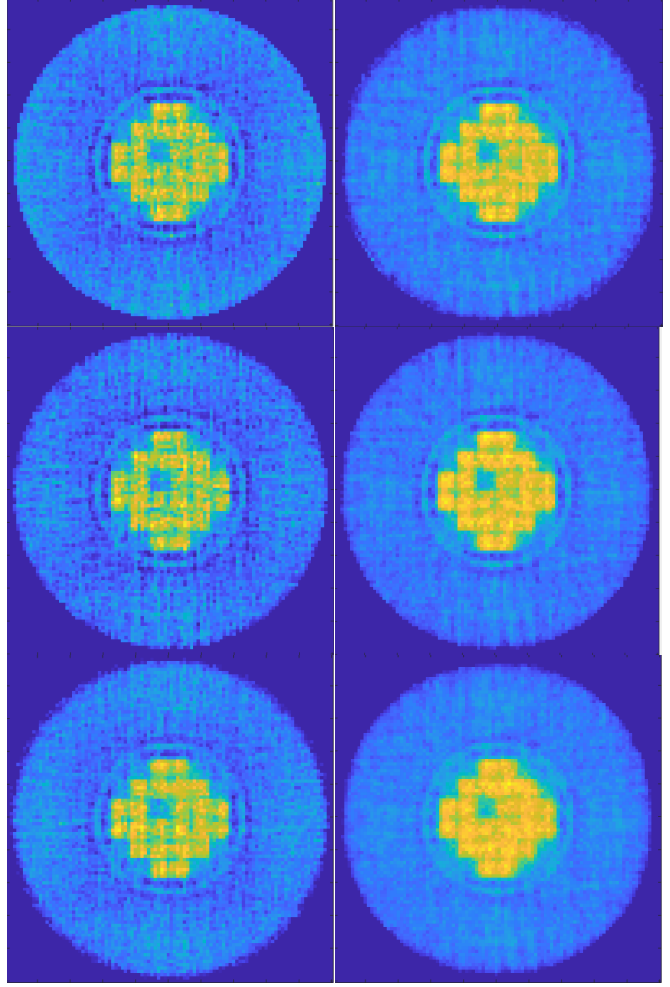


Figure 3. SIRT reconstruction of a dry cask referring Figure without momentum measurement. Results are shown using method 1a (top-left), method 2a (middle-left), method 3a (bottom-left) and method 1b (top-right), method 2b (middle-right), method 3b (bottom-right).

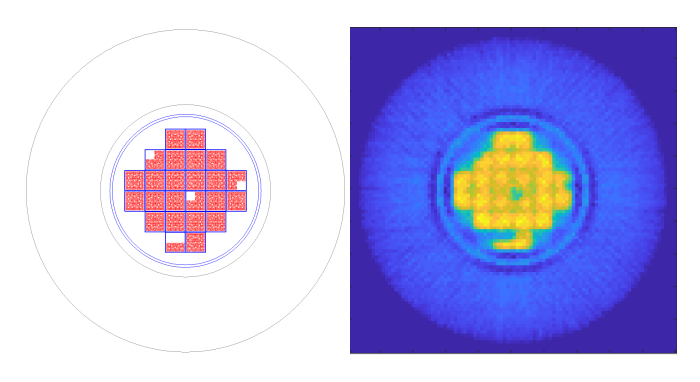
Signal to noise ratio (SNR), contrast to noise ratio (CNR) and detection power (DP) were used to access how the muon path models and projection methods would the reconstruction image quality. SNR, CNR and detection power (DP) were calculated with

 $SNR = \frac{\text{mean(8 assemblies surrounding missing one)}}{\text{std(8 assemblies surrounding missing one)}}$ $CNR = \frac{\text{mean(8 assemblies)} - \text{mean(missing one)}}{\text{max(std(8 assemblies), std(missing one))}}$ detection power = SNR * CNR

Table 9. Image characteristics for the 6 methods

	With momentum			Without momentum		
	SNR	CNR	DP	SNR	CNR	DP
	FBP					
1a	5.80	2.49	14.50	4.33	1.85	8.02
1b	6.59	2.47	16.25	5.90	1.77	10.48
	SART					
1a	10.69	4.53	48.43	7.63	3.09	24.58
2a	11.19	4.91	54.94	7.36	3.08	22.78
3a	11.21	4.94	55.38	7.36	3.92	22.74
1b	12.58	5.34	67.18	11.27	4.44	50.08
2b	12.68	5.42	68.72	10.37	4.01	41.69
3b	13.81	5.47	75.54	13.97	4.44	62.04

According to the above analysis, it can be observed that from straight path along muon incident trajectory to straight path along muon incident direction crossing PoCA point to PoCA trajectory, both reconstruction image quality and detection power are slightly improved. By back projecting muon scattering angles to the pixels crossed by its trajectory and calculating the variance of scattering angle in each pixel then taking the summation of variance along incident horizontal direction as projection information, it could significantly improve image quality and decrease the reliance on muon momentum information, which in reality is very hard to measure with traditional radiation detectors. In order to investigate the detection limit of our muon CT, a dry storage cask with half and three quarter-assemblies missing. Without losing the generality, quarter assemblies were lost at the center, between two fuel assemblies at the rim and at the edge as shown in Figure .



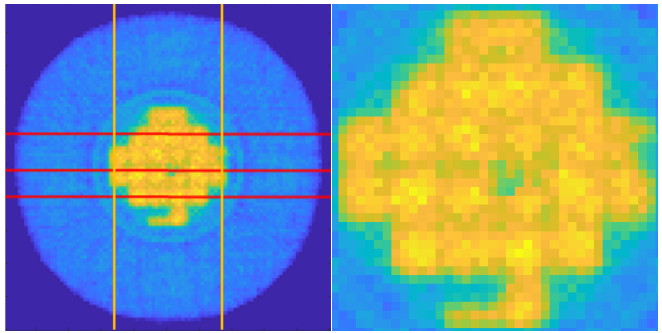
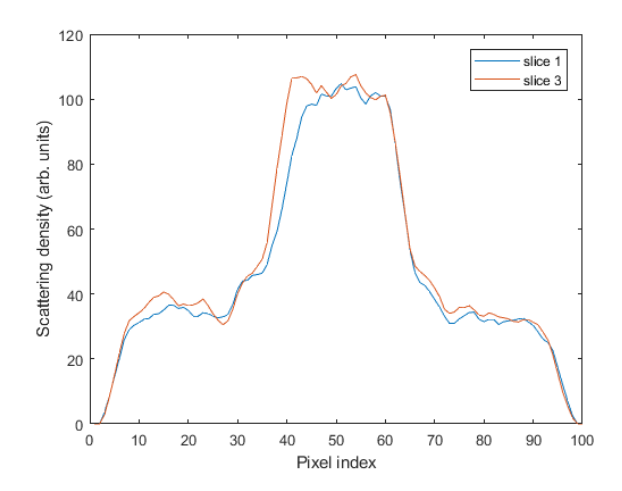


Figure 80 Top-down (top-left) view of the cask with a half assembly and 3 quarter assemblies missing and the reconstructed image using method 3b with perfect momentum information (top-right), without momentum information (bottom-left), and a zoomed-in view of the central part of the figure (bottom-right).

A quantity of 1.5×10^7 muons were to reconstruct the image with method 3b. Without any further signal processing, in both reconstructed images with and without momentum information, quarter assembly missing scenario at any location in the cask can be easily detected. Six slices crossing the reconstructed image with method 3b and no momentum were used to review the quarter assemblies missing on the rim of 24 spent nuclear fuel assemblies shown in Figure . Due to the symmetry of configuration, a comparison between slice 1 (the horizontal line at the top) and slice 3 (the horizontal line at the bottom) could be used to reveal fuel missing in the assembly on the left in that row shown in Figure at the top; similarly slice 2 (the horizontal line in the middle) revealed the missing at the center of the cask and the comparison between slice 4 (the vertical line on the left) and slice 5 (the vertical line on the right) revealed the missing in the top fuel assembly in most left column. The estimated scattering density in the missing quarter fuel slot and rest three quarters of fuel are 73.62 ± 7.7 and 101.6 ± 5.0 (arb. units), which are separated by $5.5 \, \sigma$ of the fuel assembly. Thus missing quarter fuel assembly can be distinguished from the fuel assemblies.



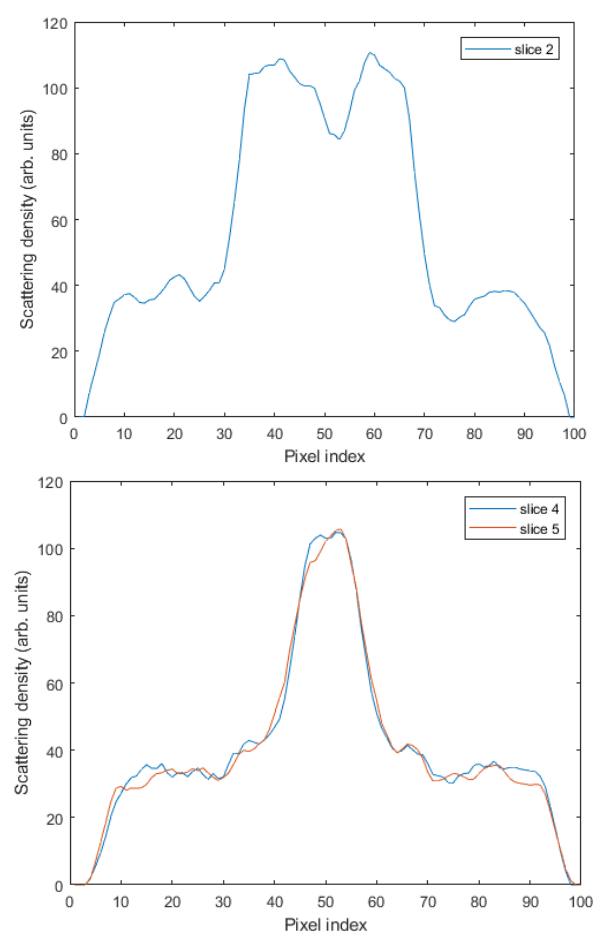


Figure 81. A comparison of the simulated slices of scattering density, showing slice 1 and 2 at the top, slice 2 in the middle and a comparison of slice 4 and 5 at the bottom. See text for details.

6.6. Detector size

Although using large area position sensitive plane detectors or ring detectors which could cover the whole cask can generate complete information of the cask wall and spent nuclear fuel in the middle, it is not economically practicable to build such large area detector with readout electronic. When small size detectors whose width is shorter than the diameter of cask are in use, placing upper detector in one of the n positions within the range (0°,180°] on the rim of cask and placing the lower detector at each of the n positions in the range (180°, 360°] can still yield same sinogram information collected with large size detectors, however, it would significantly increase the measurement time by n² fold [41]. Due to the central symmetry of the cask wall and smaller scattering density compared to spent nuclear fuel in the middle, a complete sinogram information of the whole cask is not a necessity to reconstruct the spent nuclear assemblies in the middle of the cask. Thus length of detector only needs to no smaller than the diameter of canister. 1.6×1.2 m² muon trackers were simulated to register muons crossing a VSC-24 dry with one spent nuclear fuel missing exactly similar to one described in test model configuration section except the detector size as shown on the left in Figure . Only the data registered by muon track in a 1.6×1.2 m² area in previous section was used here to reconstruct the spent nuclear fuel in center

with method 1a as shown on the right in Figure . The SNR and CNR 8.73 and 4.81, which are quite close to the image quality reconstructed with a large size detectors.

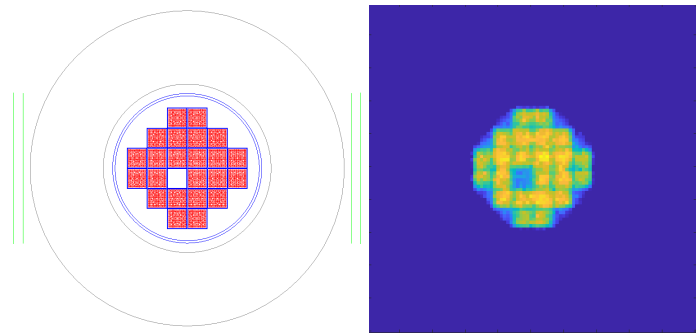


Figure 82. top-down (right) illustrations of the cask and detectors built in Geant4 and reconstructed image (left) with method 1a.

7. Summary and Conclusion

In this project, a prototype muon imaging system based on scintillation detectors were designed, constructed and tested for the purpose of monitoring used nuclear fuel content inside dry storage casks. Two detector designs (i.e. single scintillator panel and independent detector bars) were explored. Front-end electronics were designed to reduce the number of required readout. High-speed digitizers were used for data acquisition. The prototype system demonstrated imaging capability that is sufficient for the design purpose. Impact of elevated radiation background was also studied using the combination of field measurements and laboratory testing. Overall the prototype system showed encouraging results and the technical approach warrants further study.

In the algorithm aspect, three different muon trajectory models (incident trajectory, straight path along incident direction crossing PoCA point, or PoCA trajectory) along with two projection methods (project scattering angles to detector bin or project summation of scattering density to detector bins), combined together as 6 different methods, were investigated to reconstruct the expected computed tomography of a VSC-24 dry nuclear fuel storage cask. A Geant4 simulation workspace validated against the only relevant experimental data from a MC-10 dry storage cask was used. Either FBP or ART-based reconstruction methods were used to reconstruct the projected information stored in the detector bins. Algebraic techniques are more useful when particle trajectory are not straight on account of scattering or it is under sampling. When the same projection method is used, the PoCA trajectory is expected to yield better image quality and have an improved detection capability compared to the case where a straight path along the incident direction crossing the PoCA point is used, which is, in turn, better than use of a straight path along the incident horizontal trajectory. However, the expected differences observed when using different ray tracing models are not very significant. When the same muon ray tracing method is used, by back projecting the scattering to pixels crossed by its trajectory and then projecting the summation of variance of scattering angle in each pixel to corresponding detector bins, SNR, CNR and detection capability are expected to be boosted compared to the projection method of simply storing scattering angle into detector bins by at least 13 percent, 10 percent and 25 percent when perfect momentum is used, 40 percent, 13 percent and 83 percent when no momentum information is used. Then a simulated VSC-24 dry cask with portions of assemblies

missing was used to analyze the expected detection limit. Method 3b, expected to be able to detect a quarter of a missing assembly at any location in the cask, even without any momentum information, performs the best.

8. Presentations and publications

Journal publications.

- Z. Liu, C. Liao, H. Yang and J. P. Hayward, ""Detection of Missing Assemblies and Estimation of the Scattering Densities in a VSC-24 Dry Storage Cask with Cosmic-Ray-Muon-Based Computed Tomography," Journal of Nuclear Materials Management, Volume 45, No. 4, August 2017. **Published. Acknowledgement of federal support (yes).**
- S. Chatzidakis, Zhengzhi Liu, "A Generalized Muon Trajectory Estimation Algorithm with Energy Loss for Application to Muon Tomography," submitted for review to JAP. **Accepted. Acknowledgement of federal support (yes).**
- Zhengzhi Liu et al., "Ray Tracing and Reconstruction Methods in Muon-Computed Tomography of Used Nuclear Fuel in Dry Storage Casks (uCT)," in preparation. Acknowledgement of federal support (yes).
- C. Liao, H. Yang, Z. Liu and J. Hayward, "Design and Characterization of a Scintillator-Based Position-Sensitive Detector for Muon Imaging," Nuclear Technology, submitted, Acknowledgement of federal support (yes).

Other publications, conference papers and presentations.

- C. Liao, H. Yang, Z. Liu, J. P. Hayward, "A Prototype Cosmic-ray Muon Tomography System for Dry Storage Cask Monitoring," 2017 IEEE NSS/MIC Conference Record, Atlanta, Georgia, USA, 21 – 28 October, 2017, acknowledgement of federal support (yes).
- Z. Liu, S. Chatzidakis, C. Liao, H. Yang, J. P. Hayward, "Characteristics of Muon Computed Tomography of Used Fuel Casks Using Algebraic Reconstruction," 2017 IEEE NSS/MIC Conference Record, Atlanta, Georgia, USA, 21 – 28 October, 2017, acknowledgement of federal support (yes).
- Can Liao, Haori Yang, Zhengzhi Liu, Jason Hayward, A Scintillation-Fiber Based Cosmic-Ray Muon Tomography System for Imaging Dry Storage Cask, American Nuclear Society Transactions, 2016, acknowledgement of federal support (yes).
- Can Liao and Haori Yang, Design of a Cosmic-ray Muon Radiography System for Dry Storage Cask Imaging, 2014 IEEE Nuclear Science Symposium & Medical Imaging Conference Record, Seattle, WA USE, 8-15 November 2014, acknowledgement of federal support (yes).
- C. Liao, H. Yang, Z. Liu, J. P. Hayward, "Experimental Validation of a Scintillator-Based, Cosmic-ray Muon Tomography Proof-of-Concept System for Dry Nuclear Fuel Storage Cask Monitoring," 2018 Symposium on Radiation Measurements and Applications (SORMA XVII), submitted, acknowledgement of federal support (yes).
- Zhengzhi Liu et al., "MUON-COMPUTED TOMOGRAPHY USING POCA TRAJECTOY FOR IMAGING SPENT NUCLEAR FUEL IN DRY STORAGE CASKS," accepted for presentation at International Congress on Advances in Nuclear Power Plants, Charlotte, NC, 2018. acknowledgement of federal support (yes).

• S. Chatzidakis, Zhengzhi Liu, et al., "Maximum-a-Posteriori Cosmic Ray Muon Trajectory Estimation with Energy Loss for Muon Tomography Applications," IEEE Nuclear Science Symposium, Atlanta, GA, 2017. Acknowledgement of federal support (yes).

9. Training of graduate and undergraduate students

Two graduate students are currently being supported by this NEUP project.

Mr. Can Liao graduated from University of Utah with a Master degree in Nuclear Engineering. His research will cover the simulation study of muon tomography, study of scintillation detector and WLS fiber and development of image reconstruction algorithm.

Mr. Zhengzhi Liu has a bachelor's degree in Nuclear Engineering and Technology from Harbin Engineering University. Past work included research on CZT coded aperture imaging for locating radioactive sources. In this program, Zhengzhi is working on image reconstruction and will be supporting the experimental work as well.

Numerous undergraduate students were hired to work on this project as hourly employees.

Reference

- [1] W. C. Priedhorsky, et al, "Detection of high-Z objects using multiple scattering of cosmic ray muons," Rev. Sci. Instrum., Vol. 74, No. 10, pp. 4294-4297, Oct. 2003.
- [2] L. J. Schultz, et al, "Image reconstruction and material Z discrimination via cosmic ray muon radiography," Nu cl. Instr. Meth. A, Vol. 519, No. 3, pp. 687-694, Mar. 2004.
- [3] W. B. Gilboy, et al, "Industrial radiography with cosmic-ray muons: A progress report," Nucl. Instr. Meth. A, V ol. 580, No. 1, pp. 785-787, 2007.
- [4] K. Hagiwara, et al., Particle data group, review of particle physics, Phys. Rev. D 66 (1) (2002).
- [5] Richard Claude Hoch, "Advances in Cosmic Ray Muon Tomography Reconstruction Algorithms," master thesi s, College of Engineering, Florida Institute of Technology (2009).
- [6] L. J. Schultz, et al, "ML/EM Reconstruction Algorithm for Cosmic Ray Muon Tomography," 2006 IEEE Nucle ar Science Symposium Conference Record
- [7] L. J. Schultz, et al, "Statistical Reconstruction for Cosmic Ray Muon Tomography," IEEE Trans. Ima. Proc. Vo l. 16, no. 8, pp. 1985-1993, 2007
- [8] P.M. Jenneson et al, "Imaging large vessels using cosmic-ray muon energy-loss techniques," Chemical Enginee ring Journal 130 (2007) 75–78
- [9] William C. Priedhorsky et al, "Detection of high-Z objects using multiple scattering of cosmic ray muons," Rev iew of Scientific Instruments, volume 74, number 10
- [10] John Perry et al, "Imaging a nuclear reactor using cosmic ray muons," Journal of Applied Physics 113, 184909 (2013)
- [11] Z. Wang et al., "Inexpensive and practical sealed drift-tube neutron detector," Nucl. Instrum. Methods Phys. Re s. A 605(3), 430–432 (2009).
- [12] D.F. Mahon et al, "A Prototype Scintillating-Fibre Tracker for the Cosmic-ray Muon Tomography of Legacy N uclear Waste Containers," Nucl. Instrum. Methods Phys. Res. A, 723, 408-411 (2013).
- [13] H. S. Lee, et al, "Development of a Cosmic-ray Muon Radiography System with Plastic Scintillators," Korean P hys. Soc., Vol. 54, No. 5, pp. 2076-2081, May 2009.
- [14] Morris, C.L., et al., Tomographic imaging with cosmic ray muons. Science & Global Security, 2008. 16(1-2): pp. 37-53.
- [15] Gary Blanpied, "Material Discrimination Using Scattering and Stopping of Cosmic Ray Muons and Electrons a nd Detection of Gamma Radiation," 2014 IEEE NSS/MIC Conference Record
- [16] David Schwellenbach, "Imaging Shielded Configurations Using Near-Horizontal and Near-Vertical Trajectory Cosmic-Ray Muons," 2014 IEEE NSS/MIC Conference Record

- [17] Baihui Yu et al, "An MAP Algorithm with Edge-preserving Prior for Muon Tomography," 2014 IEEE NSS/MI C Conference Record
- [18] Wang, Xuewu, et al. "Design and construction of muon tomography facility based on MRPC detector for high-Z materials detection." Nuclear Science Symposium and Medical Imaging Conference (NSS/MIC), 2012 IEEE. IEEE, 2012.
- [19] Hengguan Yi et al, "Bayesian-Theory-based Most Probable Trajectory Reconstruction Algorithm in Cosmic Ra y Muon Radiography," 2014 IEEE NSS/MIC Conference Record
- [20] Debasis Mitra, "Simulation Study of Muon Scattering For Tomography Reconstruction," 2009 IEEE Nuclear Science Symposium Conference Record
- [21] Marcus Hohlmann et al, "GEANT4 Simulation of a Cosmic Ray Muon Tomography System with Micro-Patern Gas Detectors for the Detection of High-Z Materials," IEEE Transactions On Nuclear Science, Vol. 56, No. 3, June 2009
- [22] Chris Hagmann et al, "Cosmic-Ray Shower Generator (CRY) for Monte Carlo Transport Codes," 2007 IEEE N uclear Science Symposium Conference Record
- [23] Lindsay Cox et al, "Detector Requirements for a Cosmic Ray Muon Scattering Tomography System," 2008 IEE E Nuclear Science Symposium Conference Record
- [24] Chung Yau and Elton Ho, "Cosmic Ray Muon Detection using NaI Detectors and Plastic Scintillators," http://home.fnal.gov/~group/WORK/muonDetection.pdf
- [25] K. Gnanvo et al, "Detection and Imaging of High-Z Materials with a Muon Tomography Station Using GEM D etectors," 2010 IEEE NSS Conference Record
- [26] MINERvA Collaboration, The MINERvA Technical Design Report, MINERvA-doc-700-v28, December 2006
- [27] "CRIPT project web page at Carleton University". http://www.physics.carleton.ca/cript
- [28] J. Dong et al, "Large Area Position-Sensitive Plastic Scintillator Detector with Wavelength-Shifting Fiber Read out" 2014 IEEE NSS/MIC Conference Record
- [29] Ulisse Bravar et al, "Design and Testing of a Position-Sensitive Plastic Scintillator Detector for Fast Neutron Im aging," IEEE Transactions on Nuclear Science, Vol. 53, No. 6, December 2006
- [30] Evan Downie et al, "Investigation of analog charge multiplexing schemes for SiPM based PET block detectors, "Phys. Med. Biol. 58 (2013) 3943–3964
- [31] Siegel S. et al, "Simple charge division readouts for imaging scintillator arrays using a multi-channel PMT," IE EE Trans. Nucl. Sci. 43 1634–41, 1996
- [32] Gaisser, Thomas K., Ralph Engel, and Elisa Resconi. Cosmic rays and particle physics. Cambridge University P ress, 2016.
- [33] Anderson, David W. Absorption of ionizing radiation. University Park Press, 1984
- [34] V. ANGHEL et al., "A Plastic Scintillator-based Muon Tomography System with an Integrated Muon Spectrom eter," Nucl. Instrum. Methods, Phys. Res. A, 798, 12–23 (Oct. 2015).
- [35] BAESSO et al., "Toward a RPC Based Muon Tomography System for Cargo Containers," J. Instrum., 9, C1004 1 (Oct. 2014).
- [36] E. ASTROM et al., "Precision Measurements of Linear Scattering Density Using Muon Tomography," J. Instrum., 11, P07010 (Jul. 2016).
- [37] S. CHATZIDAKIS et al., "Analysis of Spent Nuclear Fuel Imaging Using Multiple Coulomb Scattering of Cosmic Muons," IEEE Trans. Nuc. Sci., 63, 2866 (2016).
- [38] J. M. DURHAM et al., "Cosmic Ray Muon Imaging of Spent Nuclear Fuel in Dry Storage Casks," J. Nucl. Mat er. Manage., 44, 3 (2016).
- [39] S. CHATZIDAKIS and L. H. TSOUKALAS, "Theoretical Investigation of Spent Nuclear Fuel Monitoring Using Cosmic Ray Muons," International Congress on Advances in Nuclear Power Plants (ICAPP 2016), San Francisco, April 17–20, 2016.
- [40] S. CHATZIDAKIS, C.K. CHOI, and L. H. TSOUKALAS, "Investigation of Imaging Spent Nuclear Fuel Dry Casks Using Cosmic Ray Muons," Trans. Am. Nucl. Soc., 114, 152–155 (2016).